Lepton portal dark matter at muon colliders: Total rates and generic features for phenomenologically viable scenarios

Adil Jueid[1,*] and Salah Nasri[2,3,†]

[1]*Center for Theoretical Physics of the Universe, Institute for Basic Science (IBS), 34126 Daejeon, Republic of Korea*
[2]*Department of Physics, United Arab Emirates University, Al-Ain 15551, United Arab Emirates*
[3]*The Abdus Salam International Centre for Theoretical Physics, Strada Costiera 11, I-34014 Trieste, Italy*

(Received 8 February 2023; accepted 24 May 2023; published 21 June 2023)

Lepton portal dark matter (DM) models are a class of models where the DM candidates solely couple to charged leptons through a mediator carrying a lepton number. These models are very interesting since they avoid constraints from direct detection experiments even for coupling of order $\mathcal{O}(1)$, they have small annihilation cross sections, and can be probed efficiently at lepton colliders. In this work, we consider a minimal lepton portal DM model that consists of extending the standard model with two $SU(2)_L$ singlets: a charged scalar singlet and an electrically neutral right-handed fermion. We systematically study the production mechanisms of DM at multi-TeV muon colliders. After considering all the possible theoretical and experimental constraints and studying the phenomenology of lepton flavor violation and DM in the muonphilic scenario, we analyze the production rates of 54 channels (26 channels for prompt DM production and 28 channels for charged scalar production) at multi-TeV muon colliders. Finally, we discuss the possible collider signatures of some channels and the corresponding backgrounds. We find that at least nine channels for DM production can be very efficient in testing DM with masses up to about 1 TeV.

DOI: 10.1103/PhysRevD.107.115027

I. INTRODUCTION

Supported by various astrophysical and cosmological observations, it is now widely accepted that dark matter (DM) exists in the Universe (see, e.g., [1–4] for comprehensive reviews). On the other hand, the measurements of the anisotropies in the cosmic microwave background implies that DM is the dominant component of the matter budget in the Universe with a density of $\Omega_{\rm DM}h^2 = 0.1198 \pm 0.0015$ [5]. The standard theories of structure formation require that the DM should be nonrelativistic at the matter-radiation equality. In particle physics models, this can be easily realized by extending the standard model (SM) with weakly interacting massive particles (WIMPs) under the standard thermal freeze-out mechanism. The search for WIMPs was one of the major programs at the Large Hadron Collider (LHC). A special characteristic of WIMPs production at the LHC is that one can probe it through the recoil of a SM particle against a large missing transverse energy ($E_T^{\rm miss}$). Examples of these processes are monojet [6], mono-Z [7,8], or mono-Higgs [9], among others. Unfortunately, various searches for WIMPs at the LHC were unsuccessful in finding such signals and limits were put on the production cross section versus the DM mass [10–14], which were interpreted in various particle physics realizations. Furthermore, these constraints were even more stringent when the void bounds from direct detection experiments [15,16] were included [17,18]. The situation is not very different in the case where the DM production is mediated through colored mediators or leptoquarks with the main mechanisms for DM density in the early Universe being the coannihilation or conversion-driven freeze-out mechanisms [19–23]. The interpretation of these searches exclude DM masses of about 0.1–1 TeV and mediator masses of about 0.5–5 TeV depending on the theoretical model.

In light of this current situation, an important question arises: what if DM only couples to the lepton sector? From the theoretical standpoint, there is *a priori* no fundamental principle that can prevent DM from coupling to leptons only. This class of models was proposed some time ago in Ref. [24] and was widely studied in the literature [25–36]. There are many interesting implications for these models. First, the scattering of the DM off the nucleus is induced at the one-loop order and therefore these models can easily

*adiljueid@ibs.re.kr
†snasri@uaeu.ac.ae
salah.nasri@cern.ch

evade direct detection constraints even for model parameters of order $\mathcal{O}(1)$. Second, except for electronphilic scenarios, constraints from positron indirect detection searches are also not important, since their annihilation is dominated by p-wave amplitudes that are suppressed by the square of the DM velocity. Finally, the DM can be produced at the LHC through the decay of charged scalars and therefore the corresponding bounds are not as strong as in the case of mono-X searches, especially in the case of $SU(2)_L$ gauge singlet mediators [30]. Therefore, an efficient probe of this category of models is through leptonic colliders such as the International Linear Collider (ILC), Chinese Electron Positron Collider (CEPC), and the future muon colliders. Recently, future muon colliders are attracting high interest due to their capability to probe new physics beyond the SM at very high scales [37–39], therefore competing with future circular colliders (FCC-hh). On the other hand, these machines can achieve very high energies thanks to the expected excellent cooling systems and the weaker synchrotron radiation. Finally, at very high energies, muon colliders are necessarily vector-boson colliders where the dominant production channels are through vector-boson fusion (VBF) [40,41]. Phenomenology of both the SM and beyond at muon colliders has been extensively studied in the literature (see, e.g., [42–62]).

In this work, we study the production of DM at muon colliders within the minimal lepton portal DM model, in which we extend the SM with two $SU(2)_L$ singlets: a charged scalar that plays the role of the mediator and a neutral right-handed fermion (or, equivalently, Majorana particle) that plays the role of the DM candidate. We first comprehensively discuss the impact of the different theoretical and experimental constraints on the model parameter space in the muonphilic scenario, i.e., the scenario where the DM couples predominantly to muons. We then select a few benchmark points that define phenomenologically viable scenarios that can be probed at high-energy muon colliders. We study the production cross sections and the expected backgrounds for a set of production channels totaling 26 production channels for DM and 28 production channels for the charged singlet scalar. A particular feature of this model is that the DM is a Majorana fermion and therefore does not couple to gauge bosons directly; therefore, the direct production of DM does not receive any contribution from VBF channels. We select a few production channels that can have high discovery potential and discuss the possible signatures and the associated backgrounds. This work is an introduction for future projects, where a complete exploration of the model at muon colliders will be performed.

The remainder of this paper is organized as follows. We discuss the model and its UV completion in Sec. II, along with the constraints from LEP searches, $H_{\rm SM} \to \gamma\gamma$, and theoretical constraints. In Sec. III, we discuss the constraints from charged lepton flavor violation in $\ell_\alpha \to \ell_\beta\gamma$, $\ell_\alpha \to 3\ell_\beta$, and $H_{\rm SM} \to \ell_\alpha\bar{\ell}_\beta$. A detailed analysis of DM phenomenology in this model is presented in Sec. IV, where we discuss the DM relic density, direct detection constraints, and Higgs invisible decays. A study of DM production at muon colliders, the interesting signatures, and the associated backgrounds is performed in Sec. V. In Sec. VI, we study the production of charged scalars at muon colliders. We draw our conclusions in Sec. VII.

II. THEORETICAL SETUP

A. The model

We consider a minimal extension of the SM by two gauge singlet fields: a charged scalar (S) and a right-handed fermion (N_R). We further assume that the two extra singlets are odd under Z_2 symmetry, while all the SM particles are even; i.e., $\{S, N_R\} \to \{-S, -N_R\}$ and $\{\ell, q, \nu, \Phi, V^\mu\} \to \{\ell, q, \nu, \Phi, V^\mu\}$. To ensure that the N_R state is a suitable DM candidate within our model, we impose the condition $M_{N_R} < M_S$. Furthermore, the charged singlet is assumed to carry a lepton number and therefore couples only to charged leptons.[1] The full Lagrangian is given by

$$\mathcal{L} = \mathcal{L}_{\rm SM} + \mathcal{L}_S - V(\Phi, S), \tag{1}$$

where Φ refers to the SM Higgs doublet, $\mathcal{L}_S$ is the interaction Lagrangian for the singlet scalar (including the kinetic term), and $V(\Phi, S)$ is the scalar potential. The interaction Lagrangian for the S field is given by

$$\mathcal{L}_S = \sum_{\ell=e,\mu,\tau} Y_{\ell N}\bar{\ell}^c_R S N_R + (\mathcal{D}^\mu S)^\dagger(\mathcal{D}_\mu S) + \text{H.c.}, \tag{2}$$

with $\mathcal{D}_\mu S = (\partial_\mu - ig_2 Y_S B_\mu/2)S$ being the covariant derivative, $Y_S = 2$ is the hypercharge of the scalar singlet, and g_2 is the $U(1)_Y$ gauge coupling. The kinetic term in Eq. (2) gives rise to interaction with A_μ and Z_μ, which are given, after field rotations, by

$$\begin{aligned}\mathcal{L}_{S;\text{gauge}} = &-(eA^\mu - e\tan\theta_W Z^\mu)S^\dagger\bar{\partial}_\mu S + e^2 A_\mu A^\mu S^\dagger S \\ &+ e^2\tan^2\theta_W Z_\mu Z^\mu S^\dagger S - 2e^2\tan\theta_W A_\mu Z^\mu S^\dagger S,\end{aligned}$$

where $e = \sqrt{4\pi\alpha_{\rm EM}}$ is the electric charge, θ_W is the Weinberg mixing angle, and $A\bar{\partial}_\mu B \equiv A(\partial_\mu B) - (\partial_\mu A)B$. The most general CP-conserving, renormalizable, and gauge invariant scalar potential is given by

[1]This charged singlet is also called a scalar lepton [63] and the relevant interaction Lagrangian is similar to the case of interaction of supersymmetric slepton with a neutralino and a charged lepton. The difference here is that we assume a single charged scalar to couple to all the leptons instead of three scalars, usually denoted by $\tilde{e}_R, \tilde{\mu}_R$, and $\tilde{\tau}_R$, where each scalar couples to a specific lepton generation.

$$V(\Phi,S) = -M_{11}^2|\Phi^\dagger\Phi| + M_{22}^2|S^\dagger S| + \lambda_1|\Phi^\dagger\Phi|^2 + \lambda_2|S^\dagger S|^2 + \lambda_3|\Phi^\dagger\Phi||S^\dagger S|. \quad (3)$$

All the parameters of the scalar potential are assumed to be real valued as a consequence of CP conservation. The process of electroweak symmetry breaking leads to three physical scalars: $H_{\rm SM}$ identified with the recently discovered 125 GeV SM Higgs boson and a pair of charged scalars denoted by $H^\pm$. Their masses are given at the lowest order in perturbation theory by

$$M_{H_{\rm SM}}^2 = \lambda_1 v^2 = 2M_{11}^2, \qquad M_{H^\pm}^2 = M_{22}^2 + \frac{1}{2}\lambda_3 v^2, \quad (4)$$

with v being the vacuum expectation value of the SM Higgs doublet. This model involves seven additional free parameters, which we parametrize as follows:

$$\{M_{H^\pm}, M_{N_R}, \lambda_2, \lambda_3, Y_{eN}, Y_{\mu N}, Y_{\tau N}\}. \quad (5)$$

For convenience, we define the combination of the couplings $Y_{\ell N}$ by[2]

$$Y_{\ell N} = \sqrt{Y_{eN}^2 + Y_{\mu N}^2 + Y_{\tau N}^2},$$

which is a very good parametrization in case the charged leptons are assumed to be massless.

B. Theoretical and experimental constraints

The parameters of the model in Eq. (5) are subject to various theoretical and experimental constraints. We start with a brief discussion of the constraints influencing the scalar potential parameters and $M_{H^\pm}$, where more details can be found in [30]. The width of the SM Higgs boson is only affected by the rate of its decay to $\gamma\gamma$. In this model, this process receives new contributions from the charged singlet scalar, which give rise to destructive or constructive contributions depending on the sign of λ_3 [64–66].[3] In the present work, we have used the most recent ATLAS-CMS combined measurement of $|\kappa_\gamma|$ [67],

$$|\kappa_\gamma| \equiv \sqrt{\Gamma(H\to\gamma\gamma)/\Gamma(H\to\gamma\gamma)_{\rm SM}} = 0.87^{+0.14}_{-0.09}.$$

We assume the theoretical prediction to be in agreement with the experimental measurement at the 2σ level. We found that the enhancement of $|\kappa_\gamma|$ always occur for $\lambda_3 < 0$, which excludes charged scalars with masses up to ~380 GeV [66]. For $\lambda_3 > 0$, we get three possible regimes: (i) large and negative contribution that implies an enhancement of κ_γ, (ii) positive but small contribution, which makes κ_γ consistent with the experimental measurement, and (iii) exact or almost exact cancellation between the $H^\pm$ and the W-boson contributions, which make κ_γ very small. Therefore, for $\lambda_3 > 0$, charged singlet masses up to 380 GeV are excluded, but with a small region where the constraints completely vanish.

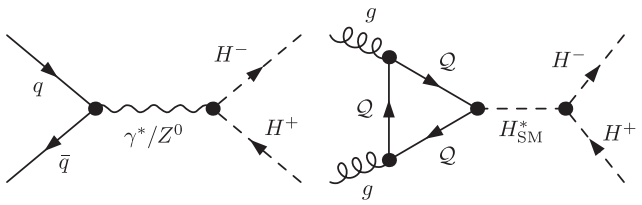

FIG. 1. Example of Feynman diagrams for the pair production of singlet scalars at the LHC. Here we show the production through $q\bar{q}$ annihilation (left) and through gg fusion which is one-loop induced (right).

In addition to constraints from Higgs decays, the parameters of the scalar potential are subject to a number of theoretical constraints. We note that the bounds on the scalar potential of this model can be obtained from those in, e.g., the inert doublet model by setting $\lambda_4 = \lambda_5 = 0$. In this study, we impose constraints from vacuum stability conditions (or boundedness from below) [68], perturbativity, perturbative unitarity [69,70], and false vacuum [71]. The false vacuum condition plays a very important role in constraining the parameters λ_2, λ_3, and $M_{H^\pm}$. We get

$$M_{H^\pm}^2 \geq \frac{1}{2}\left(\lambda_3 v^2 - M_{H_{\rm SM}}^2\sqrt{\frac{\lambda_2}{\lambda_1}}\right). \quad (6)$$

We found that (i) λ_3 cannot be larger than 5 for all charged scalar masses, and (ii) there is a parabola in the plane defined by λ_3 and $M_{H^\pm}$, which simply tells us that the smaller the minimum allowed value of $M_{H^\pm}$ is, the smaller is the maximum allowed value of λ_3. These conclusions are mildly dependent on the choice of λ_2 and, therefore, we choose $\lambda_2 = 2$ in the remainder of this manuscript without loss of generality.

The model can be constrained by using the null results of LEP and LHC searches for supersymmetric particles [72–74]. The OPAL Collaboration of the LEP experiment has searched for charginos decaying into a charged lepton and the lightest supersymmetric neutralino using 680 pb^{-1} of integrated luminosity [72]. Assuming that the branching ratio of $H^\pm \to \mu^\pm N_R$ is 100%, the production of charged singlet pairs occurs through gauge interactions (s-channel diagrams with the exchange of γ^*/Z^0). This search constrains the mass of the charged singlet to be not heavier than 100 GeV for any value of $Y_{\mu N}$. This can be seen clearly in

[2]This is equivalent to a definition of a system of spherical coordinates wherein the new parameters are $Y_{\ell N}, \theta$, and φ such that $\theta \in [0,\pi]$ and $\varphi \in [0,2\pi]$. The couplings in Eq. (2) are defined here as $Y_{eN} = Y_{\ell N}\cos\varphi\sin\theta$, $Y_{\mu N} = Y_{\ell N}\sin\varphi\sin\theta$, and $Y_{\tau N} = Y_{\ell N}\cos\theta$.

[3]We have found a typo in the analytical expression in Ref. [65] which may influences their numerical results.

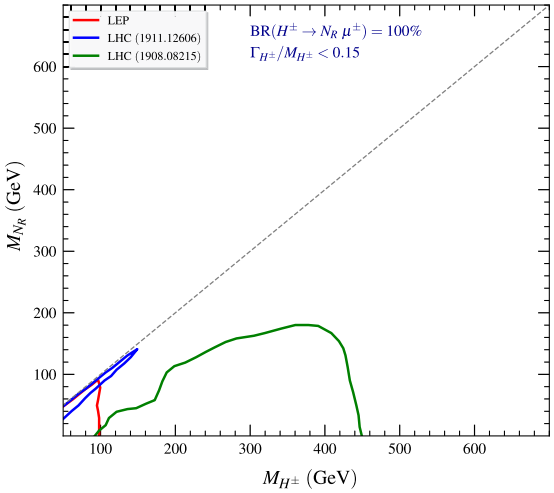

FIG. 2. Summary of the collider constraints on the parameter space of the model displayed on the plane of $(M_{H^\pm}, M_{N_R})$. We show the constraints from LEP searches of sleptons and charginos (red), LHC searches for sleptons in the compressed regime (blue), and constraints from LHC searches of sleptons and charginos for large mass splittings (green). Here, we assume that the charged singlet scalar decays to $\mu^\pm N_R$ with a branching fraction of 100% and assume the narrow width approximation by selecting parameters for which we have $\Gamma_{H^\pm}/M_{H^\pm} < 0.15$. The gray dashed line corresponds to the kinematical boundary above which the N_R particle is not a suitable dark matter candidate.

the red contour of Fig. 2. The ATLAS Collaboration at the LHC has also searched for sleptons and charginos assuming 100% branching fraction to a charged lepton and neutralino. These searches targeted large mass splitting $\Delta = m_{\tilde{\ell}} - m_{\chi^0} \geq 80$ GeV [73] and compressed spectra for a mass splitting as low as 0.55 GeV [74]. The two searches utilized a total luminosity of 139 fb^{-1}. The first search resulted in constraining the scalar singlet masses to be lighter than about 440 GeV, while the search for compressed spectra constrained the whole compressed region for $M_{H^\pm}$ up to 150 GeV (see the blue and green contours of Fig. 2).

Before closing this subsection, we comment on the effect of the gluon fusion-induced cross section on the current bounds from slepton searches. The pair production of the charged singlet scalar at the LHC proceeds through two classes of diagrams (see Fig. 1). In all the calculations, we have used the NNPDF3.0_as_0118_lo parton distribution function set [75] and have chosen the renormalization and factorization scales to be equal to the charged scalar mass; $\mu_R = \mu_F = M_{H^\pm}$. For the production through $q\bar{q}$ annihilation, we have estimated the cross section at leading order (LO) with up to two extra partons in the final state. The merging of these samples were performed using the MLM merging scheme [76]. The production cross section ranges from 81.12 fb for $M_{H^\pm} = 100$ GeV to 0.17 fb for $M_{H^\pm} = 500$ GeV. It is very important to check whether the contribution of gg fusion would affect the bounds for large values of λ_3 in the regions near the exclusion bounds. We have calculated the gluon-induced cross section taking into account both diagrams involving a gauge boson (γ/Z) and a SM Higgs boson. We found that for charged scalar masses of 400–500 GeV, the gluon-induced contribution is much smaller than the leading order Drell-Yan contribution.[4] This implies that the current bounds are not affected by the inclusion of the contribution from the gg fusion.

C. Examples of UV completions

In this section, we discuss the UV completions of this minimal framework. In general, there are two ways to UV complete the first term in $\mathcal{L}_S$: (i) assume it to be a part of a radiative neutrino mass model, or (ii) embed it in a grand unified theory, $SU(5)$ for example. We start with the radiative neutrino mass models. The most economical way to extend this model is through the so-called Krauss-Nasri-Trodden (KNT) three-loop radiative neutrino mass model [77]. In addition to S and N_R, the KNT model extends the SM with an additional scalar singlet that is even under Z_2. Another possibility is through the so-called scotogenic model, which extends the SM with one inert doublet and three right-handed fermions [78]. The phenomenology of the scotogenic model has been widely studied in the literature [79–86]. The relevant interaction becomes

$$\mathcal{L} \supset h_{\alpha\beta}\bar{L}_{L\alpha}(i\sigma_2)\Phi_{\rm IDM}N_\beta \supset h_{\alpha\beta}\overline{\ell}_{L\alpha}SN_\beta, \tag{7}$$

where $\Phi_{\text{Inert Doublet Model}} = (S, (h_2 + ia_2)/\sqrt{2})^T$, and α, β are generation indices. Identifying (7) with the first term in $\mathcal{L}_S$, we have $Y_{eN} = h_{11}, Y_{\mu N} = h_{21}, Y_{\tau N} = h_{31}$. We must stress that the gauge interactions of the singlet scalar in this model are different from the scotogenic model due to the fact that S is a member of the $SU(2)_L$ doublet, whereas it is a singlet in the present model.

The first term in Eq. (2) can be obtained from a grand unified theory; for example, by embedding the SM into a $SU(5)$ gauge group with the matter fields belonging to the $\mathbf{10}_F$ and $\bar{\mathbf{5}}_F$ representations, the charged singlet belongs to the $\mathbf{10}_H$ representation, and the right-handed neutrino belongs to the singlet representation $\mathbf{1}_\alpha$, which in this case we can write as

$$\mathcal{L}_{\rm int} = g_{\alpha\beta}\overline{\mathbf{10}}_\alpha \otimes \mathbf{10}_H \otimes \mathbf{1}_{N_\beta} \supset g_{\alpha\beta}\ell^T_{R\alpha}CN_\beta S^+. \tag{8}$$

[4]For example, the gluon-induced cross section is 0.036 fb for $\lambda_3 = 4$ and $M_{H^\pm} = 500$ GeV.

In addition to the minimal $SU(5)$, we can obtain the first term of Eq. (2) from a flipped-$SU(5) \otimes U(1)_X$ grand unified theory (GUT). Here, the right-handed charged lepton field is a singlet under $SU(5)$, whereas the right-handed neutral fermion (N_R) is a member of the $\mathbf{10}_\alpha$ representation. In this case, we have

$$\mathcal{L}_{\rm int} = \frac{h_{\alpha\beta}}{\Lambda}\overline{\mathbf{10}}_\alpha \otimes \bar{\mathbf{1}}_\beta \otimes \mathbf{10}_H \otimes \mathbf{1}_S + \text{H.c.} \supset \frac{h_{\alpha\beta}\langle \mathbf{10}_H\rangle}{\Lambda} N^T C \ell_R S^-, \tag{9}$$

where we integrated out a heavy intermediate state with a scale $\Lambda \gg \Lambda_{\rm GUT}$.

III. CHARGED LEPTON FLAVOR VIOLATION

The interaction Lagrangian in Eq. (2) conserves total lepton number to all orders in perturbation theory since the charged singlet possesses a lepton number.[5] However, the charged singlet scalar can give rise to processes violating flavor lepton numbers L_α; $\alpha = e,\ \mu,\ \tau$ at the one-loop order. These processes are called charged lepton flavor violating (CLFV) processes and are categorized into three categories: (i) $\ell_\alpha = \ell_\beta\gamma$, (ii) $\ell_\alpha \to \ell_\beta\ell_\beta\overline{\ell}_\beta$, and (iii) e–μ conversion in nuclei. In this section, we discuss the impact of the CLFV constraints on the model parameter space. The most stringent bounds on the couplings $Y_{\ell_\alpha N}$ come from the branching ratio of $\mu \to e\gamma$ decay. The analysis of the CLFV decays in this work are heavily based on the results of Refs. [87–90]. A summary of the current and future bounds on the CLFV decays is shown in Table I.

A. $\ell_\alpha \to \ell_\beta\gamma$

The radiative decays of charged leptons ($\ell_\alpha \to \ell_\beta\gamma$) receive contributions from the exchange of the charged singlet scalar and Majorana DM. After computing the one-loop integrals, we get the effective magnetic dipole operator $\mu^M_{\beta\alpha}\overline{\ell}_\beta\sigma^{\mu\nu}\ell_\alpha F_{\mu\nu}/2$ with $\mu_{\beta\alpha} = em_\alpha A_{\rm M}/2$ and $A_{\rm M}$ is given by

$$A_{\rm M} = \frac{Y_{\ell_\beta N}Y_{\ell_\alpha N}}{2(4\pi)^2}\frac{1}{M^2_{H^\pm}}\mathcal{F}(\xi),$$

where $\xi = M^2_{N_R}/M^2_{H^\pm}$ and $\mathcal{F}(x) = (1 - 6x + 3x^2 + 2x^3 - 6x^2\log x)/(6(1-x)^4)$ is the one-loop function which has the following limits $\mathcal{F}(x) \to 1/6(1/12)$ for $x \to 0(1)$. The resulting decay branching ratio can be computed easily to give

$$\text{BR}(\ell_\alpha \to \ell_\beta\gamma) = \frac{3(4\pi)^3\alpha_{\rm EM}}{4G_F^2}|A_{\rm M}|^2 \times \text{BR}(\ell_\alpha \to \ell_\beta\nu_\alpha\bar{\nu}_\beta). \tag{10}$$

Here, $G_F = 1.166 \times 10^{-5}\ \text{GeV}^{-2}$, $\alpha_{\rm EM} = 1/137$, and $\text{BR}(\ell_\alpha \to \ell_\beta\nu_\alpha\overline{\nu_\beta})$ is the SM decay branching ratio. We choose $\text{BR}(\mu \to e\nu\overline{\nu})$, $\text{BR}(\tau \to e\nu\bar{\nu})$, $\text{BR}(\tau \to \mu\nu\bar{\nu}) \approx 1$, 0.1783, 0.1741 [100].

Using the most recent experimental bounds on $\text{BR}(\ell_\alpha \to \ell_\beta\gamma)$ from the MEG [91] and *BABAR* [93] experiments, we can use Eq. (10) to derive the following bounds on the products of the couplings:

$$|Y_{eN}Y_{\mu N}| < \left(\frac{2.855\times10^{-5}}{\text{GeV}}\right)^2\frac{M^2_{H^\pm}}{|\mathcal{F}(\xi)|},$$
$$|Y_{eN}Y_{\tau N}| < \left(\frac{4.428\times10^{-4}}{\text{GeV}}\right)^2\frac{M^2_{H^\pm}}{|\mathcal{F}(\xi)|},$$
$$|Y_{\tau N}Y_{\mu N}| < \left(\frac{4.759\times10^{-4}}{\text{GeV}}\right)^2\frac{M^2_{H^\pm}}{|\mathcal{F}(\xi)|}. \tag{11}$$

Since the one-loop function varies roughly between $1/12$ and $1/6$, the upper bound on the coupling $Y_{\ell_\alpha N}Y_{\ell_\beta N}$ is proportional to the square of the charged singlet mass with almost no dependence on M_{N_R}. Therefore, limits are expected to be strong for light $H^\pm$ and become very weak for heavy $H^\pm$. This can be clearly seen in Fig. 3, where the maximum allowed values of $|Y_{\ell_\alpha N}Y_{\ell_\beta N}|$ by the CLFV decays $\text{BR}(\ell_\alpha \to \ell_\beta\gamma)$ are shown as a function of $\xi = M^2_{N_R}/M^2_{H^\pm}$ for $M_{H^\pm} = 500$, 1000, and 5000 GeV. As expected, the bounds on $|Y_{eN}Y_{\mu N}|$ are the strongest ones, while the bounds on $|Y_{\tau N}Y_{\mu N}|$ and $|Y_{eN}Y_{\tau N}|$ are similar.

TABLE I. Current experimental bounds and future sensitivities for low-energy CLFV decays and high-energy Higgs boson lepton flavor violating decays.

CLFV decay	Existing bounds	Expected projections
$\mu \to e\gamma$	5.7×10^{-13} [91]	6×10^{-14} [92]
$\tau \to e\gamma$	3.3×10^{-8} [93]	$\sim 10^{-8} - 10^{-9}$ [94]
$\tau \to \mu\gamma$	4.4×10^{-8} [93]	$\sim 10^{-8} - 10^{-9}$ [94]
$\mu \to eee$	1.0×10^{-12} [95]	$\sim 10^{-16}$ [96]
$\tau \to eee$	2.7×10^{-8} [97]	$\sim 10^{-9} - 10^{-10}$ [94]
$\tau \to \mu\mu\mu$	2.1×10^{-8} [97]	$\sim 10^{-9} - 10^{-10}$ [94]
$H_{\rm SM} \to \mu\tau$	1.5×10^{-3} [98]	⋯
$H_{\rm SM} \to e\tau$	2.2×10^{-3} [98]	⋯
$H_{\rm SM} \to e\mu$	3.5×10^{-4} [99]	⋯

[5]To generate a Majorana neutrino mass one has extend the Lagrangian (2) so that the total lepton number is violated. The minimal realization of such breaking can be achieved by having, in addition to S, a second $SU(2)$ singlet charged scalar with lepton number equals to two units; which is the KNT model.

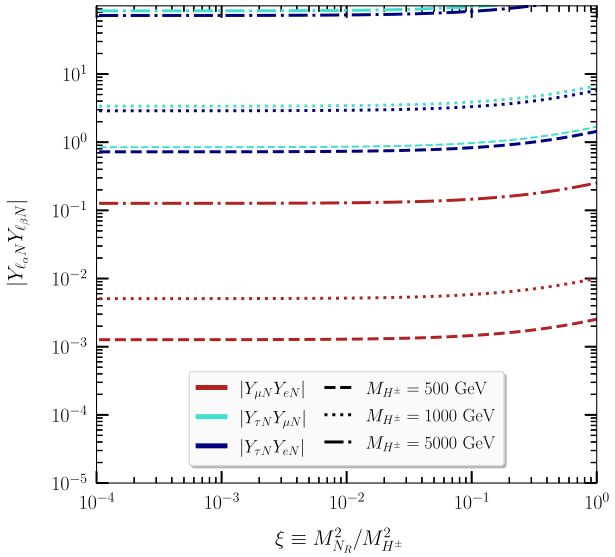

FIG. 3. The maximum value of the products of the $Y_{\ell_\alpha N}Y_{\ell_\beta N}$ as a function of ξ for different values of the charged singlet mass $M_{H^\pm}$. The results are shown for $M_{H^\pm} = 500$ GeV (dashed), $M_{H^\pm} = 1000$ GeV (dotted), and $M_{H^\pm} = 5000$ GeV (dash-dotted).

We must stress that the experimental bounds on the CLFV processes constrain the product $|Y_{\ell_\alpha N}Y_{\ell_\beta N}|$ and not each coupling $Y_{\ell_\alpha N}$ separately. Following this finding, there is some freedom regarding the choice of the couplings, which we call here benchmark scenarios (see next sections). Given that this study is mainly concerned about the phenomenology of the leptophilic DM models at muon colliders, we choose a scenario where the coupling of dark matter to the muon is quite large, whereas the other couplings are chosen such that they fulfill the experimental bounds on CLFV decays: $Y_{\mu N} \simeq \mathcal{O}(1) \gtrsim Y_{\tau N} \gg Y_{eN}$.

B. $\ell_\alpha \to \ell_\beta \ell_\beta \bar{\ell}_\beta$

It is worth discussing the constraints from the CLFV decays $\ell_\alpha \to \ell_\beta \ell_\beta \bar{\ell}_\beta$. These processes receive four contributions at the one-loop order: penguin diagrams with the exchange of γ, Z, and $H_{\rm SM}$ and box diagrams. The contribution of the SM Higgs boson is suppressed due to the smallness of the Higgs-lepton Yukawa coupling. The corresponding branching ratio is given by [90]

$$\mathrm{BR}(\ell_\alpha \to \ell_\beta \ell_\beta \bar{\ell}_\beta) = \frac{3(4\pi)^2\alpha_{\rm EM}}{8G_F^2}\Bigg[\overbrace{|A_{\rm ND}|^2 + |A_{\rm M}|^2\left(\frac{16}{3}\log\left(\frac{m_\alpha}{m_\beta}\right) - \frac{22}{3}\right)}^{\gamma\ \text{penguin}} + \overbrace{\frac{1}{3}(2|Z_{\rm RR}|^2 + |Z_{\rm RL}|^2)}^{Z\ \text{penguin}} + \frac{1}{6}|B_{\rm box}|^2 + \underbrace{2\mathrm{Re}\left(-2A_{\rm ND}A_{\rm M}^* + \frac{1}{3}A_{\rm ND}B_{\rm box}^* - \frac{2}{3}A_{\rm M}B_{\rm box}^*\right)}_{\text{Interference}}\Bigg] \times \mathcal{B}, \tag{12}$$

where $\mathcal{B} \equiv \mathrm{BR}(\ell_\alpha \to \ell_\beta \nu_\alpha \bar{\nu}_\beta)$. The contribution of the γ penguins consists of the magnetic or dipole ($A_{\rm M}$) nd the nondipole ($A_{\rm ND}$) contributions. The dipole contribution is the same as for $\mathrm{BR}(\ell_\beta \to \ell_\beta \gamma)$, but is enhanced by a factor of $16 \times (\log(m_\alpha/m_\beta) - 22)/3$, which varies between 7 and 36 for $\tau \to 3\mu$ and $\tau \to 3e$, respectively. The nondipole contribution is given by

$$A_{\rm ND} = \frac{Y_{\ell_\alpha N}Y_{\ell_\beta N}}{6(4\pi)^2}\frac{1}{M^2_{H^\pm}}\mathcal{G}(\xi),$$

with $\mathcal{G}(x) = (2 - 9x + 18x^2 - 11x^3 + 6x^3\log x)/(6(1-x)^4)$ being the one-loop function for the nondipole γ penguin. This function has the following limits: $\lim_{x\to 0}\mathcal{G}(x) = 1/3$ and $\lim_{x\to 1}\mathcal{G}(x) = 1/4$. Therefore, the dipole γ-penguin contribution is large as compared to the nondipole contributions; $\lim_{x\to 0}(\lim_{x\to 1})A_{\rm M}/A_{\rm ND} \times (16/3\log(m_\alpha/m_\beta) - 22/3) \approx \{3.5, 11, 18\}(\{2, 7, 12\})$ for $\tau \to 3\mu, \mu \to 3e$, and $\tau \to 3e$, respectively. The Z-penguin contribution is given by

$$Z_{\rm RR} = \frac{g_R^\ell Z_{\rm ND}}{g_1^2\sin^2\theta_W M_Z^2}, \qquad Z_{\rm RL} = \frac{g_L^\ell Z_{\rm ND}}{g_1^2\sin^2\theta_W M_Z^2}, \tag{13}$$

where g_R^ℓ, g_L^ℓ are the right- and left-handed components of the Z-boson couplings to charged leptons, g_1 is the $SU(2)_L$ gauge coupling, $\sin\theta_W$ is the sine of the Weinberg mixing angle, and $Z_{\rm ND}$ is the momentum-independent Z-boson form factor, which is given by

$$Z_{\rm ND} = \frac{Y_{\ell_\alpha N}Y_{\ell_\beta N}}{2(4\pi)^2}\frac{m_\alpha m_\beta}{M^2_{H^\pm}}\frac{g_1}{\cos\theta_W}\mathcal{F}(\xi).$$

We can see that the Z-penguin contribution involves an extra suppression by a factor of $m_\alpha m_\beta$ as compared to the dipole γ contribution. Finally, the box contribution is given by

$$B_{\rm box} = \frac{Y_{\ell_\alpha N}Y^3_{\ell_\beta N}}{2^7\pi^3\alpha_{\rm EM}M^2_{H^\pm}}[\mathcal{D}_1(\xi) + 2\xi\mathcal{D}_2(\xi)], \tag{14}$$

where $\mathcal{D}_{1,2}(x)$ are the one-loop box functions given by $\mathcal{D}_1(x) = (-1 + x^2 - 2x\log x)/(1-x)^3$ and $\mathcal{D}_2(x) = (-2 + 2x - (1+x)\log x)/(1-x)^3$. The contribution of the box diagrams, contrary to penguins, has an extra factor of $Y^2_{\ell_\beta N}$. Therefore, it may dominate for large couplings of the daughter lepton to DM. In this work, we check that the benchmark scenarios satisfy the bounds from the $\ell_\alpha \to 3\ell_\beta$ decays (see Table II).

C. $H_{\rm SM} \to \ell_\alpha \bar{\ell}_\beta$

We close this section by a brief discussion of the CLFV decays of the SM Higgs boson. These decays have been searched for by the ATLAS and the CMS Collaborations, with the strongest bounds reported by THE CMS Collaboration [98,99]. In this model, the CLFV decays of the SM Higgs boson are degenerate to the radiative CLFV decays of the charged leptons. The constraints from CLFV of charged leptons imply that the CLFV decays of the SM Higgs boson are extremely suppressed and may even be beyond the future reach of the LHC and future colliders. The SM Higgs boson decay into $\ell_\alpha \ell_\beta$ is given by [101]

$$\mathrm{BR}(H_{\rm SM} \to \ell_\alpha \ell_\beta) \simeq 1.2 \times 10^3 \times |y_{\ell_\alpha} Y_{\ell_\alpha N} Y_{\ell_\beta N}|^2 \times \left(\frac{\lambda_3}{4\pi}\right)^2 \left(\frac{v}{M_{H^\pm}}\right)^4, \tag{15}$$

where $y_{\ell_\alpha} = m_{\ell_\alpha}/(\sqrt{2}v)$ is the Higgs-lepton Yukawa coupling of the heavier lepton (chosen here to be ℓ_α). In this formula, the contribution of the lighter lepton is neglected. We expect the bounds from $H_{\rm SM} \to \ell_\alpha \bar{\ell}_\beta$ searches to be very weak. This can be clearly seen in Table II for the benchmark points we have used in this study.

IV. DARK MATTER

In this section, we discuss the DM phenomenology within this model. We start with the calculation of the relic density of the N_R particles in Sec. IV A and then move to a detailed analysis of the spin-independent DM-nucleus scattering cross section in Sec. IV B. Next, we derive the constraint on the couplings Y_{lN} by analyzing the Higgs invisible decays and conclude by a selection of the benchmark points that are compatible with all the theoretical and experimental constraints in Sec. IV D.

A. Relic density

The relic density of the N_R particles receives contributions from both the annihilation and the coannihilation. The coannihilation becomes active when the mass splitting $\Delta \equiv M_{H^\pm} - M_{N_R} < 0.1 \times M_{N_R}$, whereas the annihilation contributes for the whole parameter space. For the annihilation, there are two major contributions: (i) $N_R N_R \to \ell^+_\alpha \ell^-_\beta$ from the exchange of the charged scalar singlet in t and u channels, and (ii) $N_R N_R \to \sum_{X\in \rm SM} X\bar{X}$, which arises from the exchange of the SM Higgs boson via s-channel diagrams. Note that s-channel contributions to the relic density are negligible in our model if one demands perturbativity of the couplings. The reason is that the leading order contribution to the s-channel annihilation amplitudes arises at the one-loop order.

To obtain the relic density of the N_R particles, one must solve the Boltzmann equations given by [1,102,103]

$$\frac{\mathrm{d}n_{N_R}}{\mathrm{d}t} + 3Hn_{N_R} = -2\langle\sigma_{N_R} v\rangle[(n_{N_R})^2 - (n^{\rm eq}_{N_R})^2], \tag{16}$$

where $H = \dot{a}/a$, n_{N_R} is the number density of the N_R particle and $n^{\rm eq}_{N_R} \approx g_{N_R}(\frac{M_{N_R}T}{2\pi})^{3/2} e^{-M_{N_R}/T}$ is its number density in the thermal equilibrium. Note that, in the absence of interactions that change the number density of N_R, the right-handed side of Eq. (16) would be equal to zero and $n_{N_R} \propto a^{-3}$. This equation can be solved to give approximately

$$\Omega_{\rm DM}h^2 \simeq \frac{3\times 10^{-27}\ \mathrm{cm^3\ s^{-1}}}{\langle\sigma(x_f)v\rangle}, \tag{17}$$

where $\langle\sigma(x_f)v\rangle$ is the thermally averaged annihilation cross section for the N_R particle,

$$\langle\sigma(x_f)v\rangle = \frac{1}{8M^4_{N_R}T_f K^2_2(M_{N_R}/T_f)} \sum_{\alpha,\beta} \int_{4M^2_{N_R}}^{\infty} \mathrm{d}\hat{s}\, \sqrt{\hat{s} - 4M^2_{N_R}} \times K_1(\sqrt{\hat{s}}/T_f)\sigma_{N_R N_R \to \ell_\alpha \ell_\beta}(\hat{s}), \tag{18}$$

where $K_1(x)$ and $K_2(x)$ are the modified Bessel functions of the second kind and $\sigma_{N_R N_R \to \ell_\alpha \ell_\beta}(\hat{s})$ is the annihilation cross section into charged lepton, which is given by

$$\sigma_{N_R N_R \to \ell_\alpha \ell_\beta}(\hat{s}) = \frac{1}{2^3\pi} \frac{|Y_{\ell_\alpha N} Y_{\ell_\beta N}|^2}{\hat{s}\hat{\kappa}_1} \left[(m^2_{\ell_\alpha} + m^2_{\ell_\beta})(\hat{s} - 2M^2_{N_R}) + \frac{1}{6}\frac{\hat{\kappa}_2}{\hat{\kappa}_1}\hat{s}(\hat{s} - 4M^2_{N_R}) \right], \tag{19}$$

where $\hat{\kappa}_i \equiv \hat{\kappa}_i(M^2_{H^\pm}, M^2_{N_R}, \hat{s})$, $\hat{\kappa}_1(x,y,z) = (2x + 2y - z)^2$, and $\hat{\kappa}_2(x,y,z) = (4x - 4y + z)^2 - 2z^2$. To simplify the discussion about the relic density, we consider the annihilation cross section in the limit $\hat{s} \to 4M^2_{N_R}$,

$$\sigma_{N_R N_R \to \ell_\alpha \ell_\beta} \approx \frac{|Y_{\ell_\alpha N} Y_{\ell_\beta N}|^2}{2^6\pi M^4_{H^\pm}} (m^2_{\ell_\alpha} + m^2_{\ell_\beta}) \left(1 + \frac{M^2_{N_R}}{M^2_{H^\pm}}\right)^{-2}.$$

This equation simply tells us that the contribution of the annihilation to the relic density becomes very small for a

very heavy charged singlet scalar and, in this case, one needs to have large $Y_{\ell N}$ to produce the correct relic density. On the other hand, for large values of the mass splitting and heavy charged singlet scalar, one cannot reproduce the correct relic abundance if one demands perturbativity of the couplings.

The coannihilations are more involved in this model as we can have additional contributions that have different dependence on the model parameters. There are two generic coannihilation channels: $N_R H^\pm \to \text{SM}$ and $H^\pm H^\mp \to \text{SM}$. Below, we list the individual contributions and the overall dependence of the corresponding cross section,

$$\begin{aligned}
N_R H^\pm \to \ell_\alpha^\pm H_{\rm SM}&: \ \sigma \propto \lambda_3^2 Y_{\ell_\alpha N}^2,\\
N_R H^\pm \to \ell_\alpha^\pm Z,\quad \ell_\alpha^\pm \gamma,\quad \nu W^\pm&: \ \sigma \propto Y_{\ell_\alpha N}^2,\\
H^\pm H^\mp \to \ell_\alpha^\pm \ell_\beta^\mp&: \ \sigma \propto |Y_{\ell_\alpha N} Y_{\ell_\beta N}|^2 \mathcal{A}_1 + |Y_{\ell_\alpha N} Y_{\ell_\beta N}| \mathcal{A}_2 + \mathcal{A}_3,\\
H^\pm H^\mp \to q\bar{q}&: \ \sigma \propto \lambda_3^2 \mathcal{B}_1 + \lambda_3 \mathcal{B}_2 + \mathcal{B}_3,\\
H^\pm H^\mp \to ZZ,\quad H_{\rm SM} Z,\quad W^\pm W^\mp&: \ \sigma \propto \lambda_3^2 \mathcal{C}_1 + \lambda_3 \mathcal{C}_2 + \mathcal{C}_3,\\
H^\pm H^\mp \to H_{\rm SM} H_{\rm SM}&: \ \sigma \propto \lambda_3^4 \mathcal{D}_1 + \lambda_3^2 \mathcal{D}_2,
\end{aligned}$$

where $\mathcal{A}_i$, $\mathcal{B}_i$, $\mathcal{C}_i$, and $\mathcal{D}_i$ are real-valued coefficients that depend on the dark matter mass, the charged singlet scalar mass, and the final-state particles. The coannihilation becomes very active for quite large λ_3 and $Y_{\ell N}$ and may even drive the relic density to very small values ($\sim$ orders of magnitudes smaller than the observed abundance). In general, the coannihilation is dominated by contributions of the following two processes: $H^\pm H^\mp \to 2H_{\rm SM}$ and $N_R H^\pm \to \ell_\alpha^\pm H_{\rm SM}$. In the presence of coannihilations, the Boltzmann equations become

$$\frac{dn_{N_R}}{dt} + 3Hn_{N_R} = -2\langle \sigma_{\rm eff} v_r \rangle [(n_{N_R})^2 - (n_{N_R}^{\rm eq})^2] + N\Gamma_{H^\pm} n_{H^\pm}, \tag{20}$$

$$\frac{dn_{H^\pm}}{dt} + 3Hn_{H^\pm} = -\Gamma_{H^\pm} n_{H^\pm}, \tag{21}$$

where N is the mean number of N_R particles, $n_{H^\pm}$ is the number density of $H^\pm$, and $\Gamma_{H^\pm}$ is its total width. Note that here we have replaced the thermally averaged annihilation cross section in Eq. (16) by the effective cross section

$$\langle \sigma_{\rm eff} v_r \rangle = \sum_{i,j \in \{N_R, H^\pm\}} \langle \sigma(ij \to \text{SM}) v_r \rangle \frac{n_i^{\rm eq} n_j^{\rm eq}}{(n_{N_R}^{\rm eq})^2}. \tag{22}$$

The relic density of N_R is obtained from the numerical solutions of the coupled Boltzmann equation (21). MadDM version 3.0 is used to solve the Boltzmann equations and compute the relic density of N_R [104]. In Fig. 4, we show the values of the coupling $Y_{\ell N}$ consistent with the measurement of the relic density by the Planck Collaboration projected on the mass of the dark matter and the mass of the charged singlet scalar. We can see that the relic abundance of the N_R is consistent with the Planck measurement only for very specific regions. If the mass splitting between $H^\pm$ and N_R is large, we need large values of the $Y_{\ell N}$. However, even for $Y_{\ell N}$ near the perturbativity bound the mass splitting cannot be arbitrary large: $\Delta_{\rm max} \approx 600(2000)$ GeV for $M_{N_R} = 10(100)$ GeV. The relic density becomes almost independent of $Y_{\ell N}$ for large M_{N_R} in the coannihilation regions. We conclude this section by noting that the model cannot reproduce the correct relic density with the standard freeze-out mechanism for the region marked in blue in Fig. 4, as it breaks the perturbativity of the coupling $Y_{\ell N}$.

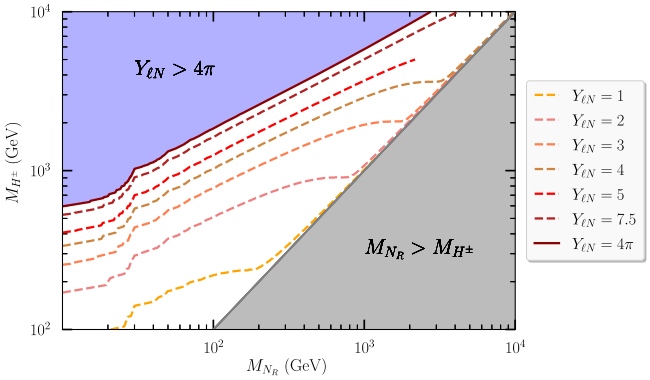

FIG. 4. Values of the coupling $Y_{\ell N}$ consistent with the measurement of the relic density by the Planck Collaboration projected on the mass of the dark matter and the mass of the charged singlet scalar. The isolines corresponding to $\Omega h^2 \approx 0.12$ are shown for $Y_{\ell N} = 1$, 2, 3, 4, 5, 7.5, and 4π. The blue shaded area corresponds to the region where the perturbativity is broken, whereas the shaded gray region corresponds to the kinematically forbidden region $M_{N_R} > M_{H^\pm}$, in which N_R is not stable and therefore not a suitable dark matter candidate.

B. Direct detection

We turn now to the discussion of the constraints from direct detection experiments on the model parameter space. In this model, the scattering cross section of N_R off the nucleus with atomic number (A) occurs at one-loop order, where the SM Higgs boson plays the role of a portal. The generic formula for the spin-independent cross section is given by[6]

$$\sigma_{\rm SI} = \frac{4}{\pi}\mu_A^2 (Z\cdot\mathcal{S}_p + (A-Z)\cdot\mathcal{S}_n)^2, \tag{23}$$

with $\mathcal{S}_{p,n}$ being the scalar current nucleon (p/n) form factors and where $\mu_A \equiv M_{N_R} m_A/(M_{N_R}+m_A)$ is the reduced mass of the N_R–A system. The nucleon form factors have two contributions: (i) from particle physics, which is connected to the scattering amplitude of the $N_R - (q/g)$ process, and (ii) from low-energy nuclear physics that are computed using chiral perturbation theory [106–109].

The generic formula of $f_{p,n}$ is given by

$$\mathcal{S}_{p,n} = m_{p,n}\sum_{u,d,s}\frac{\mathcal{A}_q}{m_q}\mathcal{S}^q_{p,n} + \frac{2}{27}m_{p,n}\mathcal{S}^g_{p,n}\sum_{c,b,t}\frac{\mathcal{A}_q}{m_q}, \tag{24}$$

where $m_p = 938.27$ and $m_n = 939.56$ MeV are the proton and neutron masses, respectively. The values of the scalar nucleon low-energy form factors are chosen to be [110]

$$\mathcal{S}^u_p = 1.53\times10^{-2}, \quad \mathcal{S}^d_p = 1.91\times10^{-2}, \quad \mathcal{S}^s_p = 4.47\times10^{-2}, \quad \mathcal{S}^g_p = 1-\sum_{q=u,d,s}\mathcal{S}^q_p = 92.09\times10^{-2},$$
$$\mathcal{S}^u_n = 1.10\times10^{-2}, \quad \mathcal{S}^d_n = 2.73\times10^{-2}, \quad \mathcal{S}^s_n = 4.47\times10^{-2}, \quad \mathcal{S}^g_n = 1-\sum_{q=u,d,s}\mathcal{S}^q_n = 91.70\times10^{-2}.$$

At the parton level, the scattering amplitude reads

$$\mathcal{M}_{qN_R\to qN_R} = \mathcal{A}_q\bar{\psi}_q(p_{\rm out})\psi_q(p_{\rm in}), \tag{25}$$

where $\mathcal{A}_q$ is connected to the nonhadronic part of the amplitude. The term $\bar{\psi}_q(p_{\rm out})\psi_q(p_{\rm in})$ should be incorporated in a hadronic current $\langle\mathcal{N}|\cdot|\mathcal{N}\rangle$,

$$\langle\mathcal{N}|\bar{\psi}_q\psi_q|\mathcal{N}\rangle = \begin{cases}\frac{m_\mathcal{N}}{m_q}\cdot\mathcal{S}^q_\mathcal{N}, & \text{for } q=u,d,s,\\ \frac{2}{27}\frac{m_\mathcal{N}}{m_q}\cdot\mathcal{S}^g_\mathcal{N}, & \text{for } q=c,b,t,\end{cases} \tag{26}$$

where $\mathcal{N} = p, n$. The model-dependent nonhadronic form factor is given by

$$\mathcal{A}_q = \frac{\tilde{y}(Q^2\approx0)}{M^2_{H_{\rm SM}}}\cdot\frac{m_q}{v}\bar{\psi}_{N_R}(k_{\rm out})\psi_{N_R}(k_{\rm in}), \tag{27}$$

where $\tilde{y}(Q^2\approx0)$ is the effective $H_{\rm SM}N_RN_R$ coupling computed in the low-energy limit. With the help of the PackageX [111], we can obtain it with the use of Eq. (30),

$$\tilde{y}(Q^2\approx fv0) \simeq -\frac{\lambda_3 v|Y_{\ell N}|^2}{16\pi M_{H^\pm}}\frac{1}{\varrho_N}[1-(1-\varrho_N^{-2})\log(1-\varrho_N^2)]$$
$$\equiv -\frac{\lambda_3 v|Y_{\ell N}|^2}{16\pi M_{H^\pm}}\mathcal{H}(\varrho_N), \tag{28}$$

where $\varrho_N = M_{N_R}/M_{H^\pm}$. Here, $\mathcal{H}(x)$ is a monotonous and increasing function of x in the interval [0, 1] and has the following limits $\lim_{x\to0}\mathcal{H}(x) = 0$ and $\lim_{x\to1}\mathcal{H}(x) = 1$. Note that the first limit corresponds to a small dark matter mass and a heavy charged scalar for which the model cannot reproduce the correct relic abundance, while the second limit corresponds to the nearly degenerate scenario, where coannihilation is the most active component in the relic abundance calculation. In addition, the effective coupling involves an extra suppression by $1/M_{H^\pm}$, which simply means that the direct detection spin-independent cross section is always below the neutrino floor for heavy $H^\pm$. From Eq. (28), one also expects that the spin-independent cross section is always proportional to $|Y_{\ell N}|^4$. Therefore, large $Y_{\ell N}$ regions with large $\sigma_{\rm SI}$ would also correspond to small relic density (which is proportional to $1/|Y_{\ell N}|^4$)[7] and for these scenarios $\sigma_{\rm SI}$ needs to be scaled by a factor $\xi_{\rm Planck} \equiv \Omega_{N_R}h^2/\Omega_{\rm Planck}h^2$. This implies that the spin-independent cross section would always be consistent with the current Xenon 1T bounds [15] for most regions of the parameter space, as can be seen clearly in Fig. 5.

C. Higgs invisible decay

The Higgs invisible decay occurs at the one-loop level with the exchange of the charged scalar and right-handed fermion. The partial decay width is given by

[6]The spin-dependent cross section is very small in our model, as the exchanged particle is the SM Higgs boson, which is a scalar particle with $J^P = 0^+$. Nevertheless, we will compute this observable for some benchmark scenarios and estimate their consistency with the current bounds from the PICO experiment [105].

[7]This is consistent with our previous finding in [30] where a strong anticorrelation between $\sigma_{\rm SI}$ and $\Omega_{N_R}h^2$ was observed.

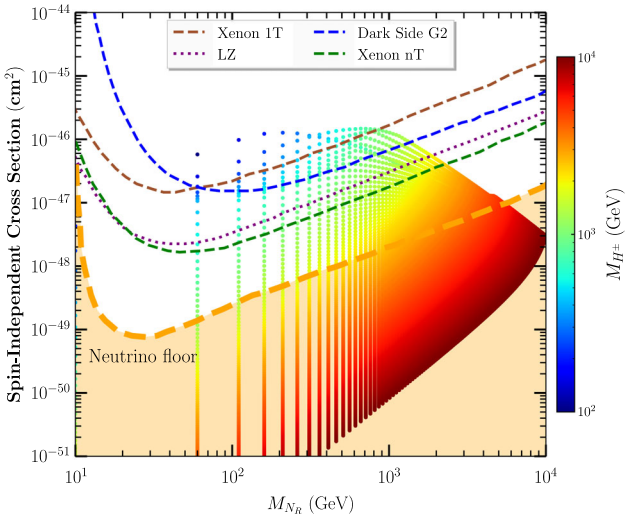

FIG. 5. The spin-independent cross section as function of the dark matter mass M_{N_R}; the colored scatter points correspond to the charged singlet scalar mass $M_{H^\pm}$. In the same plot, we show the current bounds from Xenon 1T [15] in dashed sienna and the future expectations from Xenon nT [112], LUX LZ [113], and DarkSide G2 [114]. The shaded orange area marked by "neutrino floor" corresponds to the backgrounds from the coherent scattering with solar neutrinos, atmospheric neutrinos, and supernova neutrinos [115]. The spin-independent cross section was scaled by a factor of $\xi_{\rm Planck} = \Omega_{N_R}h^2/\Omega_{\rm Planck}h^2$ with $\Omega_{\rm Planck}h^2 \approx 0.12$. All the calculations were performed for $Y_{\ell N} = 2$ and $\lambda_3 = 4$.

$$\Gamma(H_{\rm SM} \to N_R N_R) = \frac{M_{H_{\rm SM}}|\tilde{y}|^2}{8\pi}\left(1 - \frac{4M_{N_R}^2}{M_{H_{\rm SM}}^2}\right)^{3/2}, \quad (29)$$

with $\tilde{y}$ as the one-loop-induced effective $H_{\rm SM}$–N_R–N_R coupling, which is given by

$$\tilde{y} = \frac{\lambda_3 v M_{N_R}}{16\pi^2}\sum_\ell |Y_{\ell N}|^2 (C_0 + C_2), \quad (30)$$

with $C_i \equiv C_i(M_{N_R}^2, M_{H_{\rm SM}}^2, M_{N_R}^2, m_\ell^2, M_{H^\pm}^2, M_{H^\pm}^2)$, $i = 0,\ 2$ being the Passarino-Veltman three-point functions [116]. The computation of the Feynman amplitudes has been performed using FeynArts, FormCalc, and LoopTools [117,118]. We have used a Python interface to LoopTools to evaluate numerically the one-loop integrals.[8] We define the Higgs invisible branching ratio as

$$B_{\rm inv} \equiv \frac{\Gamma(H_{\rm SM} \to N_R N_R)}{\Gamma(H_{\rm SM} \to N_R N_R) + \Gamma_H^{\rm SM}}, \quad (31)$$

where $\Gamma_H^{\rm SM} = 4.07$ MeV. Using Eqs. (29)–(31), we can obtain bounds on the coupling $Y_{\ell N}$. The bound is analytically defined by

$$Y_{\ell N} < \left(\frac{2048\pi^5 \Gamma_H^{\rm SM}}{\beta_N^{3/2} M_{H_{\rm SM}} \lambda_3^2 v^2 M_{N_R}^2 |C_0 + C_2|^2 \left(\frac{1}{B_{\rm bound}} - 1\right)}\right)^{1/4},$$

where $\beta_N \equiv (1 - 4M_{N_R}^2/M_{H_{\rm SM}}^2)$ and $B_{\rm bound}$ is the upper bound on $\rm BR_{inv}$.

Searches for Higgs invisible decays have been carried out by ATLAS and CMS Collaborations [119–121]. The strongest and most up-to-date bound on $\rm B_{inv}$ was reported by the CMS Collaboration using a combination of previous Higgs to invisible decay searches at 7, 8, and 13 TeV, where it has been found that $B_{\rm inv} < B_{\rm bound} = 0.19$ at 95% C.L. [121], assuming that the rates of the Higgs boson production are equal to the SM predictions. On the other hand, several groups have performed global analyses using recent Higgs boson measurements and obtained stringent limits [122,123]. Finally, several studies have been devoted to the projected sensitivities of the future collider experiments to Higgs invisible decays from HL–LHC [124], FCC-ee [125], ILC [126], CEPC [127], and FCC-hh [128]. In Fig. 6, we show the excluded values of $Y_{\ell N}$ from present and future bounds on $\rm BR_{inv}$ assuming $M_{H^\pm} = 500$ GeV (left panel) and $M_{H^\pm} = 1000$ GeV (right panel) with $\lambda_3 = 4$. As we can see, the present bounds are extremely weak, which excludes $Y_{\ell N} \sim 6$ for $M_{N_R} \sim$ 49 GeV. The future experiments are expected to exclude smaller values of the coupling $Y_{\ell N}$; e.g., FCC-hh can exclude values up to 0.7 for $M_{N_R} \sim 49$ GeV.

D. Benchmark points

From the discussions in Secs. II and IV, we can conclude the following:

(i) The scalar singlet cannot be lighter than 440 GeV for mass splittings with dark matter mass ≤ 80 GeV.
(ii) CLFV can constrain only the product of the Yukawa-type couplings and not their individual values. So, benchmark points have to be chosen.
(iii) DM direct detection constraints are not very strong, as expected, since the spin-independent cross section is induced at the one-loop level.
(iv) The constraints from the consistency with the measurement of the DM relic density forbids large mass splittings if the Yukawa-type couplings are of order $\mathcal{O}(1)$.

The benchmark points used in the discussion of the general features of DM production at muon colliders are shown in Table II. There are four of these benchmarks and each one has its own phenomenological implications.

1. BP1

This benchmark point is characterized by a relatively light DM ($M_{N_R} = 50$ GeV) and a charged singlet mass near the exclusion limit reported by the LHC (see Fig. 2). On the other hand, the Yukawa-type couplings are chosen such

[8] PYLOOPTOOLS is a Python binding to LoopTools and can be found in this GitHub directory: https://github.com/djukanovic/pylooptools.git.

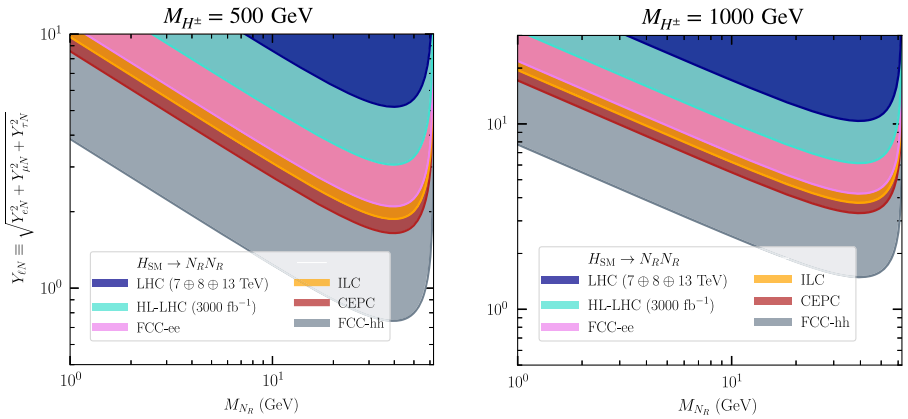

FIG. 6. The present and future exclusions on values of $Y_{\ell N}$ for $M_{H^\pm} = 500$ GeV and $\lambda_3 = 4$. Here we show the contours obtained from the LHC (navy), HL-LHC (turquoise), FCC-ee (magenta), ILC (orange), CEPC (dark red), and FCC-hh (gray). All the bounds were obtained assuming SM Higgs boson mass of $M_{H_{\rm SM}} = 125$ GeV and SM Higgs boson production rates. The Higgs diphoton rate is assumed to be equal to the SM prediction at LO.

that $Y_{\mu N} \gg Y_{\tau N} > Y_{eN}$. This choice leads to a charged scalar decaying predominantly into μN_R with a branching fraction approaching 100%. On the other hand, the charged lepton flavor violating decays are such that $\mathrm{BR}(\tau \to e\gamma)$ is well below the sensitivity reach of foreseeable future experiments. The other branching ratios are below the current experimental bounds, but can be tested in the near future. For DM observables, the relic density for this BP is about 90% of the observed abundance and the spin-independent DM-nucleon cross section is below the Xenon1T bound and the expected DarkSide G2 bound, but can be excluded or discovered by LZ.

2. BP2

For this point, we choose $M_{H^\pm} = 500$ and $M_{N_R} = 200$ GeV. The Yukawa-type couplings are chosen using the same hierarchy as BP1 but with relatively different values, i.e., $Y_{\mu N} = 1.6$, $Y_{\tau N} = 5 \times 10^{-1}$, and $Y_{eN} = 5 \times 10^{-4}$. This leads to the following branching ratios $\mathrm{BR}(H^\pm \to \mu^\pm N_R) \simeq 91\%$, $\mathrm{BR}(H^\pm \to \tau^\pm N_R) \simeq 9\%$, and $\mathrm{BR}(H^\pm \to e^\pm N_R) \simeq 0\%$. The charged scalar is narrow in this case, as $\Gamma_{H^\pm}/M_{H^\pm} \simeq 0.04$. The CLFV decays of charged leptons exhibit similar features as in BP1, with the exception that BRs of $\tau \to \mu\gamma$ and $\mu \to e\gamma$ can be probed in the future experiments, as they are slightly below the current bounds. The spin-independent DM-nucleon cross section can be probed by the DarkSide G2 experiment.

3. BP3

For this point, we choose the following values of the particle masses: $M_{H^\pm} = 600$ and $M_{N_R} = 598$ GeV, and therefore a small mass splitting of 2 GeV. We select the following values for the Yukawa-type couplings: $\{Y_{\mu N}, Y_{\tau N}, Y_{eN}\} = \{1, 0.5, 10^{-3}\}$, which leads to the following branching fractions: $\mathrm{BR}(H^\pm \to \mu^\pm N_R) \simeq 90\%$, $\mathrm{BR}(H^\pm \to \tau^\pm N_R) \simeq 10\%$, and $\mathrm{BR}(H^\pm \to e^\pm N_R) \simeq 0\%$. In this case, the branching ratios of CLFV decays of $\mu \to e\gamma$ and $\tau \to \mu\gamma$ can be tested in future experiments. Since the mass splitting is equal to 2 GeV, the most important component in the calculation of the relic density comes from coannihilation-based freeze-out and therefore the choice of λ_3 is pivotal in this case. For this BP, the relic density of the N_R is found to be below 2% of the total observed DM relic density. Finally, this BP is not sensitive to the direct detection experiments and the cross section is above the neutrino floor.

4. BP4

Here, we choose relatively heavy DM and charged scalar: $M_{N_R} = 1000$ and $M_{H^\pm} = 1500$ GeV. The Yukawa-type couplings are chosen such that $Y_{\mu N} = Y_{\tau N} = 2 \gg Y_{eN} = 5 \times 10^{-3}$. With this choice, one gets $\mathrm{BR}(H^\pm \to \mu^\pm N_R) \simeq \mathrm{BR}(H^\pm \to \tau^\pm N_R) \simeq 50\%$, while $\mathrm{BR}(H^\pm \to e^\pm N_R)$. Similar features to BP1 and BP2 are observed for CLFV and DM phenomenology.

We close this section with a qualitative discussion of the running of the parameter λ_3 for the benchmark scenarios that we study in this paper. The running of λ_3 can be determined by solving the renormalization group equations (RGEs), which are given by

$$(4\pi)^2 \frac{\mathrm{d}\lambda_3}{\mathrm{d}t} \equiv \beta_{\lambda_3}, \tag{32}$$

where $t = \log(Q^2)$ and $\beta_{\lambda_3} = \beta_{\lambda_3}^{(1)} + \cdots$ is the beta function for λ_3, which is given at one-loop order by

TABLE II. Characteristics of the four benchmark points in our model. Here, we show the values of the independent parameters, the decay branching ratios, and total width of the charged singlet scalar, the CLFV decay branching ratios, and dark-matter observables. A check mark (✓) indicates that the parameter point yields a smaller $\sigma_{\rm SI}$ than the experimental bound (present or expected), whereas an ✗ indicates that $\sigma_{\rm SI}$ is above the experimental bound.

Benchmark point	BP1	BP2	BP3	BP4
		Parameters		
M_{N_R}(GeV)	50	200	598	1000
$M_{H^\pm}$(GeV)	500	500	600	1500
Y_{Ne}	10^{-4}	5×10^{-4}	10^{-3}	5×10^{-3}
$Y_{N\mu}$	2.8	1.6	1	2
$Y_{N\tau}$	5×10^{-2}	5×10^{-1}	5×10^{-1}	2
λ_3	4	5	5	6
		Decays of $H^\pm$		
$\mathrm{BR}(H^\pm\to eN_R)$	1.27×10^{-9}	8.89×10^{-8}	8.98×10^{-7}	3.12×10^{-6}
$\mathrm{BR}(H^\pm\to \mu N_R)$	99.96×10^{-2}	91.10×10^{-2}	89.70×10^{-2}	50.0×10^{-2}
$\mathrm{BR}(H^\pm\to \tau N_R)$	3.18×10^{-4}	8.89×10^{-2}	10.29×10^{-2}	49.99×10^{-2}
$\Gamma_{H^\pm}$(GeV)	76.45	19.72	5.88×10^{-4}	73.68
$\Gamma_{H^\pm}/M_{H^\pm}$	15.29×10^{-2}	3.94×10^{-2}	9.81×10^{-7}	4.91×10^{-2}
		$\mathrm{BR}(\ell_\alpha\to\ell_\beta\gamma)$ and $\mathrm{BR}(\ell_\alpha\to3\ell_\beta)$		
$\mathrm{BR}(\mu\to e\gamma)$	2.68×10^{-14}	1.51×10^{-13}	4.31×10^{-14}	1.89×10^{-13}
$\mathrm{BR}(\tau\to e\gamma)$	1.52×10^{-18}	2.64×10^{-15}	1.92×10^{-15}	3.38×10^{-14}
$\mathrm{BR}(\tau\to \mu\gamma)$	1.17×10^{-9}	2.64×10^{-8}	1.87×10^{-9}	5.28×10^{-9}
$\mathrm{BR}(\mu\to eee)$	1.47×10^{-16}	8.21×10^{-16}	2.27×10^{-16}	1.01×10^{-15}
$\mathrm{BR}(\tau\to eee)$	1.51×10^{-20}	2.58×10^{-17}	1.85×10^{-17}	3.29×10^{-16}
$\mathrm{BR}(\tau\to \mu\mu\mu)$	1.21×10^{-8}	9.79×10^{-9}	2.63×10^{-12}	1.17×10^{-9}
		$\mathrm{BR}(H_{\rm SM}\to\ell_\alpha\ell_\beta)$		
$\mathrm{BR}(H_{\rm SM}\to \mu\tau)$	2.31×10^{-8}	1.18×10^{-6}	2.22×10^{-7}	5.24×10^{-7}
$\mathrm{BR}(H_{\rm SM}\to e\tau)$	2.95×10^{-17}	1.15×10^{-13}	2.22×10^{-13}	3.27×10^{-12}
		Dark matter observables		
$\Omega_{N_R}h^2$	9.84×10^{-2}	9.25×10^{-2}	2.11×10^{-3}	8.53×10^{-2}
$\langle\sigma v\rangle(\mathrm{cm}^2)$	2.40×10^{-9}	2.55×10^{-9}	7.32×10^{-8}	2.69×10^{-9}
$\sigma^p_{\rm SI}(\mathrm{cm}^2)$	1.60×10^{-47}	3.45×10^{-47}	2.28×10^{-48}	1.47×10^{-46}
$\sigma^p_{\rm SD}(\mathrm{cm}^2)$	6.51×10^{-62}	6.29×10^{-62}	1.98×10^{-65}	8.29×10^{-60}
		Existing bounds		
XENON1T	✓	✓	✓	✓
PICO	✓	✓	✓	✓
		Expected projections		
DarkSide G2	✓	✗	✓	✗
LZ	✗	✗	✓	✗
Neutrino floor	✗	✗	✗	✗

$$\beta^{(1)}_{\lambda_3} = \frac{27}{100}g_1^4 - \frac{9}{10}g_1^2g_2^2 + \frac{9}{4}g_2^4 - 4(Y_{eN}^2 + Y_{\mu N}^2 + Y_{\tau N}^2) \times \mathrm{Tr}(y^h_\ell y^{h,\dagger}_\ell) + \lambda_3[2(\lambda_1+\lambda_2) + 4\lambda_3 - \frac{9}{5}g_1^2 - 4g_2^2 + 2\mathrm{Tr}(y^h_\ell y^{h,\dagger}_\ell + y^h_d y^{h,\dagger}_d + y^h_u y^{h,\dagger}_u) + 2(Y_{eN}^2 + Y_{\mu N}^2 + Y_{\tau N}^2)], \quad (33)$$

where g_1 and g_2 are the gauge couplings, and y^h_f is the Yukawa matrix of the SM fermion $f=\ell,d,u$. We have used SARAH version 4.15 [129,130] to calculate the beta functions for the model parameters. From the above expression, one can see that the terms proportional to λ_3 can drive this coupling toward nonperturbativity at higher energies. Approximate solution to the RGEs leads to values of the Landau pole for this model around 10^5–10^7 GeV.

A possible solution to this issue would be a UV completion of the model at the energy scales where nonperturbativity is reached. As it was mentioned already in Sec. II, the model itself is not UV complete as it does not address, for example, the neutrino mass problem; nevertheless, this model is very simple in terms of the scaling of physical observables. The only observables that are affected by the choice of λ_3 are the spin-independent DM-nucleus cross section, the Higgs boson invisible decay width, and the mono-Higgs production cross section, which scale as λ_3^2. Reducing the value of λ_3 from, say, 4 to 2 would reduce the constraints on the spin-independent cross section and the mono-Higgs production rate by a factor of 4 and that of the Higgs invisible decay by a factor of $\sqrt{2}$.

V. PRODUCTION OF DARK MATTER AT MUON COLLIDERS

A. Total cross sections

In this section, we discuss the general features of DM production at muon colliders.[9] In this model, DM can be produced through a variety of processes:

(i) DM production in association with one SM particle dubbed as mono-X. Given the nature of the interaction Lagrangian and the fact that the initial state has a zero total electric charge, DM can only be produced in association with one neutral boson. Therefore, we have mono-γ, mono-Z, and mono-Higgs (a full analysis of these channels will be done in future work [133]).

(ii) DM production in association with two SM particles. For this category, we have seven different processes. The rates of those processes are slightly smaller than the mono-X production channels. However, these processes have smaller backgrounds (a full analysis of these channels will be done in future work [134]).

(iii) DM production in association with three SM particles. The rates of the $N_R N_R$ in association with three SM particles are even smaller than the other two categories. The signal-to-background optimizations for these channels are even more complicated, whereas the backgrounds, on the other hand, are extremely small.

In Fig. 7, we show the total cross sections for DM production in $\mu\mu$ collisions as a function of the center-of-mass energy ($\sqrt{s_{\mu\mu}}$) for the four benchmark points defined in Table II. Starting with mono-X processes, it is clear that the mono-γ channel has the highest rate, with cross section varying from $\simeq$1 pb for $\sqrt{s_{\mu\mu}} = 3$ TeV to about 80 fb for $\sqrt{s_{\mu\mu}} = 30$ TeV in BP1.[10] Mono-Z production has the second highest cross section, which varies between 200 fb for $\sqrt{s_{\mu\mu}} = 3$ TeV and about 2 fb for $\sqrt{s_{\mu\mu}} = 30$ TeV. Finally, mono-Higgs production has the lowest rates among all the mono-X processes with cross section approaching 63 fb for $\sqrt{s_{\mu\mu}} = 3$. The rates for mono-X decrease by about a factor of 10 for BP2, by a factor of 100 for BP3, and by a factor of 10 for BP4. Notice that the decrease in the production cross sections is not only due to the DM mass but also to the change in the value of $Y_{\mu N}$, since the total rates are proportional to $Y_{\mu N}^4$. An exception to this rule is in the mono-Higgs production cross section, which decreases by factors of 6–200 since it scales as $\lambda_3^2 Y_{\mu N}^4$.

The rates of the production of DM in association with two SM particles are shown in Fig. 7. We can see that, as expected, they are suppressed as compared to the case of mono-X channels. The process with the highest rate is $N_R N_R + \gamma\gamma$, whose cross section is between 50 and 2 fb. This process is followed by $N_R N_R \gamma Z$ and $N_R N_R W^+ W^-$, whose cross sections are slightly smaller. An interesting process is the production of DM in association with two SM Higgs bosons, whose cross sections are about 1–3 fb depending on the center-of-mass energy.

Finally, the production cross sections of DM in association with three SM particles are shown in Fig. 7 for BP1–BP4. It is clear that these rates are suppressed as compared to those of the DM production in association with one SM particle and two SM particles, respectively, with the maximum cross section of about 1 fb for $N_R N_R W^+ W^- \gamma$ and $N_R N_R \gamma\gamma\gamma$ at $\sqrt{s_{\mu\mu}} = 3$ TeV. We note that the dependence on $\sqrt{s_{\mu\mu}}$ of the cross sections for the production of $N_R N_R$ in association with three SM particles is not as strong as in the case of other processes. Despite the smallness of these cross sections, these processes may have a high sensitivity reach due to the smallness of the associated backgrounds.

B. Expected event yields and dominant backgrounds

After discussing the total cross sections for all the possible production channels of dark matter at muon colliders, it is instructive to discuss both the total expected number of events for specific decay channels of the SM particles and the associated backgrounds. In this subsection, we focus on two categories of DM production channels: (i) DM production in association with one SM particle, where we consider four processes: $N_R N_R \gamma$, $N_R N_R Z(\to \ell\ell)$, $N_R N_R Z(\to q\bar{q})$, and $N_R N_R H_{\rm SM}(\to b\bar{b})$ and (ii) DM production in association with two SM

[9]The cross sections for both DM and charged scalar production at muon colliders are computed at leading order using MadGraph_aMC@NLO [131] with a Universal FeynRules Output model file [132] that can be found in the FeynRules model database https://feynrules.irmp.ucl.ac.be/wiki/MinimalLeptonPortalDM.

[10]Note that for mono-γ, we have applied some generator-level cuts by requiring that $p_T^\gamma > 25$ GeV and $|\eta^\gamma| < 2.5$.

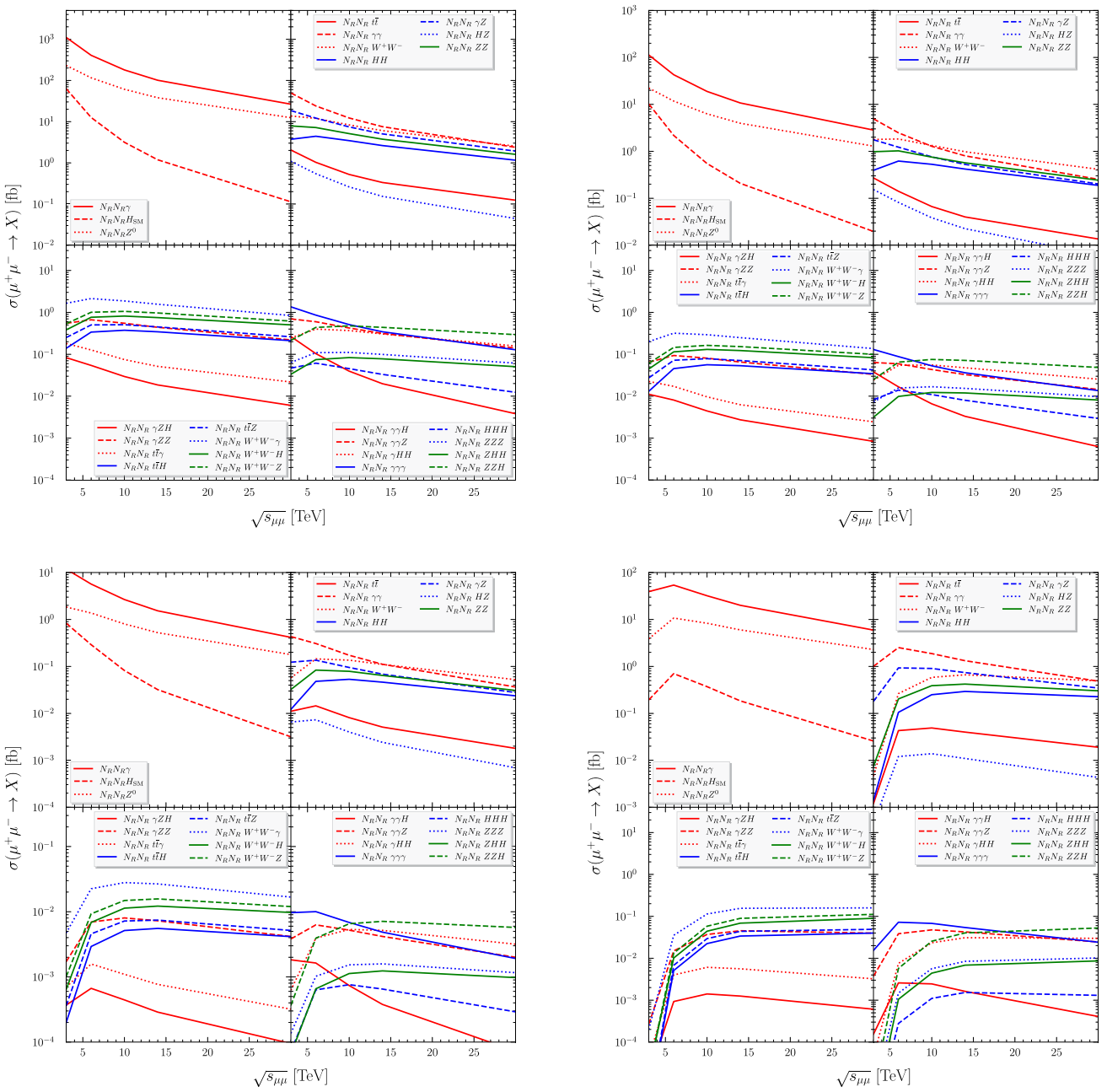

FIG. 7. Production cross section of $N_R N_R + X$ as a function of the center-of-mass energy ($\sqrt{s_{\mu\mu}}$) for the benchmark points BP1 (left upper panel), BP2 (right upper panel), BP3 (left lower panel), and BP4 (right lower panel). For each pane, we show the production cross section for $N_R N_R$ plus one SM particle, plus two SM particles and in association with three SM particles.

particles, where we consider five processes: $N_R N_R \gamma\gamma$, $N_R N_R \gamma Z(\to \ell\ell)$, $N_R N_R Z(\to \ell\ell) Z(\to \ell\ell)$, $N_R N_R V(\to q\bar{q}) V(\to q\bar{q})$, and $N_R N_R H_{\rm SM}(\to b\bar{b}) H_{\rm SM}(\to b\bar{b})$. The results are shown in Tables III and IV. The discussion will be restricted for the following center-of-mass energies and integrated luminosities

$$\sqrt{s_{\mu\mu}} = 3,\ 10,\ \text{and } 30 \text{ TeV}$$
$$\int d\mathcal{L} = 1,\ 10,\ \text{and } 90 \text{ ab}^{-1}, \tag{34}$$

where we follow Ref. [45], assuming that the luminosity has a linear scaling with the center-of-mass energy. The expected number of events for mono-X processes is calculated using the following equation:

$$\mathcal{N} = \sigma_{N_R N_R X} \times \text{BR}_{X \to x_1 x_2} \times \int d\mathcal{L}. \tag{35}$$

For the production of DM in association with two SM particles, we have

TABLE III. The total cross sections times the branching ratio ($\sigma \times \mathrm{BR}$) and the expected number of signal events for the $N_R N_R$ production in association with γ, $Z(\to \ell\ell)$, $Z(\to q\bar{q})$, and $H_{\mathrm{SM}}(\to b\bar{b})$. We consider three representative center-of-mass energies of 3, 10, and 30 TeV. For each process, we show four entries that correspond to the benchmark points considered in this study along with the associated background contributions (bkgs). Here ℓ refers to either an electron or a muon.

		$\sigma \times \mathrm{BR}$ (fb) (number of events)		
		3 TeV	10 TeV	30 TeV
$N_R N_R + \gamma$	BP1	$1.11 \times 10^3 (1.11 \times 10^6)$	$1.80 \times 10^2 (1.80 \times 10^6)$	$2.38 \times 10^1 (2.65 \times 10^6)$
	BP2	$1.13 \times 10^2 (1.13 \times 10^5)$	$1.88 \times 10^1 (1.88 \times 10^5)$	$2.83 \times 10^0 (2.55 \times 10^5)$
	BP3	$1.18 \times 10^1 (1.18 \times 10^3)$	$2.65 \times 10^0 (2.65 \times 10^4)$	$0.41 \times 10^0 (3.69 \times 10^4)$
	BP4	$3.92 \times 10^1 (3.95 \times 10^4)$	$3.20 \times 10^1 (3.20 \times 10^5)$	$5.94 \times 10^0 (5.35 \times 10^5)$
	bkgs	$3.02 \times 10^3 (3.02 \times 10^6)$	$3.29 \times 10^3 (3.29 \times 10^7)$	$3.36 \times 10^3 (3.02 \times 10^8)$
$N_R N_R + Z(\to \ell\ell)$	BP1	$1.68 \times 10^1 (1.68 \times 10^4)$	$4.44 \times 10^0 (4.44 \times 10^4)$	$0.91 \times 10^0 (8.19 \times 10^4)$
	BP2	$1.62 \times 10^0 (1.62 \times 10^3)$	$0.46 \times 10^0 (4.58 \times 10^3)$	$9.39 \times 10^{-2} (8.45 \times 10^3)$
	BP3	$0.13 \times 10^0 (0.13 \times 10^3)$	$0.58 \times 10^{-1} (0.58 \times 10^3)$	$1.30 \times 10^{-2} (1.17 \times 10^3)$
	BP4	$0.28 \times 10^0 (0.28 \times 10^3)$	$0.61 \times 10^0 (0.61 \times 10^4)$	$0.17 \times 10^0 (1.53 \times 10^4)$
	bkgs	$2.75 \times 10^1 (2.75 \times 10^4)$	$2.57 \times 10^1 (2.57 \times 10^5)$	$4.69 \times 10^1 (4.22 \times 10^6)$
$N_R N_R + Z(\to q\bar{q})$	BP1	$1.59 \times 10^2 (1.59 \times 10^5)$	$4.20 \times 10^1 (4.20 \times 10^5)$	$8.61 \times 10^0 (7.75 \times 10^5)$
	BP2	$1.53 \times 10^1 (1.53 \times 10^4)$	$4.33 \times 10^0 (4.33 \times 10^4)$	$0.89 \times 10^0 (8.00 \times 10^4)$
	BP3	$1.26 \times 10^0 (1.26 \times 10^3)$	$0.55 \times 10^0 (5.54 \times 10^3)$	$0.12 \times 10^0 (1.11 \times 10^4)$
	BP4	$2.67 \times 10^0 (2.67 \times 10^3)$	$5.73 \times 10^0 (5.73 \times 10^4)$	$1.57 \times 10^0 (1.41 \times 10^5)$
	bkgs	$4.76 \times 10^2 (4.76 \times 10^5)$	$6.71 \times 10^2 (6.71 \times 10^6)$	$1.01 \times 10^3 (0.91 \times 10^8)$
$N_R N_R + H_{\mathrm{SM}}(\to b\bar{b})$	BP1	$2.05 \times 10^1 (2.05 \times 10^4)$	$1.02 \times 10^0 (1.02 \times 10^4)$	$3.67 \times 10^{-2} (3.30 \times 10^3)$
	BP2	$5.83 \times 10^0 (5.83 \times 10^3)$	$0.31 \times 10^0 (0.31 \times 10^4)$	$1.12 \times 10^{-2} (1.01 \times 10^3)$
	BP3	$0.47 \times 10^0 (0.47 \times 10^3)$	$0.47 \times 10^{-1} (0.47 \times 10^3)$	$1.81 \times 10^{-3} (1.63 \times 10^2)$
	BP4	$0.11 \times 10^0 (0.11 \times 10^3)$	$0.21 \times 10^0 (0.21 \times 10^4)$	$1.47 \times 10^{-2} (1.32 \times 10^3)$
	bkgs	$4.76 \times 10^2 (4.76 \times 10^5)$	$6.71 \times 10^2 (6.71 \times 10^6)$	$1.01 \times 10^3 (0.91 \times 10^8)$

$$\mathcal{N} = \sigma_{N_R N_R XY} \times \mathrm{BR}_{X \to x_1 x_2} \times \mathrm{BR}_{Y \to y_1 y_2} \times \int \mathrm{d}t \mathcal{L}. \quad (36)$$

1. $\mu^+\mu^- \to N_R N_R + X$

$N_R N_R + \gamma$.—This process leads to the final state composed of a highly energetic photon and a large missing transverse energy (E_T^{miss}). In addition, one could have a few extra charged leptons or photons that are radiated from either the initial-state muons or the final-state photon. The dominant backgrounds for this signal process are the production of two or four neutrinos in association with a photon. The production of two neutrinos proceeds via muon-muon annihilation [$\mu^+\mu^- \to Z(\to \nu\bar{\nu})\gamma$] and the VBF process [$VV \to Z(\to \nu\bar{\nu})\gamma$] with cross sections varying from 2.98 pb for $\sqrt{s_{\mu\mu}} = 3$ TeV to 3.27 pb for $\sqrt{s_{\mu\mu}} = 30$ TeV. The production of four neutrinos in association with hard photons has a tiny cross section, with the maximum being 1.5 fb for $\sqrt{s_{\mu\mu}} = 30$ TeV. It is worth noting from Table III that the signal-to-background ratio ($\mathcal{S}/\mathcal{B}$) for this process varies generally between 10^{-4} and 0.3 depending on the benchmark point and the center-of-mass energy. Therefore, the signal significance can easily reach five for most of the benchmark points.[11] A detailed analysis of the monophoton signature has been performed at the parton level by the authors of Ref. [45], where they pointed out the importance of the photon energy and photon angle in discriminating between the signal and the backgrounds.

$N_R N_R + Z(\to \ell\ell)$.—This process leads to a very clean final state containing two same-flavor opposite-sign (SFOS) charged leptons from the decay of the Z boson in association with large missing energy. The dominant backgrounds are found to be the production of two Z bosons with one decaying to two charged leptons and the other decaying invisibly and the production of the two W bosons both decaying leptonically. The total cross section for the background processes can be roughly estimated as

$$\sigma(\ell\ell + E_T^{\mathrm{miss}}) \approx 2\sigma(ZZ) \times \mathrm{BR}(Z \to \ell\ell) \times \mathrm{BR}(Z \to \bar{\nu}\nu) + \sigma(WW) \times \mathrm{BR}(W \to \ell\nu)^2. \quad (37)$$

[11]The signal significance is defined as $\mathcal{S}/\sqrt{\mathcal{B}}$ with $\mathcal{S}$ as the number of signal events and $\mathcal{B}$ as the number of background events.

TABLE IV. Same as in Table III, but $N_R N_R$ in association with $\gamma\gamma$, $\gamma Z(\to \ell\ell)$, $Z(\to \ell\ell)Z(\to \ell\ell)$, $V(\to q\bar{q})V(\to q\bar{q})$, and $H_{\rm SM}(\to b\bar{b})H_{\rm SM}(\to b\bar{b})$. Here V refers to either W or Z.

		$\sigma \times$ BR (fb) (number of events)		
		3 TeV	10 TeV	30 TeV
$N_R N_R + \gamma\gamma$	BP1	$4.97 \times 10^{1}(4.97 \times 10^{4})$	$1.23 \times 10^{1}(1.23 \times 10^{5})$	$2.38 \times 10^{0}(2.38 \times 10^{5})$
	BP2	$4.93 \times 10^{1}(4.93 \times 10^{3})$	$1.28 \times 10^{0}(1.28 \times 10^{4})$	$0.25 \times 10^{0}(2.53 \times 10^{4})$
	BP3	$0.43 \times 10^{0}(0.43 \times 10^{3})$	$0.17 \times 10^{0}(1.73 \times 10^{3})$	$0.36 \times 10^{-1}(3.64 \times 10^{3})$
	BP4	$1.00 \times 10^{0}(1.00 \times 10^{3})$	$1.87 \times 10^{0}(1.87 \times 10^{4})$	$0.48 \times 10^{0}(4.85 \times 10^{4})$
	bkgs	$8.73 \times 10^{1}(8.73 \times 10^{4})$	$1.04 \times 10^{2}(1.04 \times 10^{6})$	$1.12 \times 10^{2}(1.12 \times 10^{7})$
$N_R N_R + \gamma Z(\to \ell\ell)$	BP1	$1.24 \times 10^{0}(1.24 \times 10^{3})$	$0.49 \times 10^{0}(4.98 \times 10^{3})$	$1.29 \times 10^{-1}(1.29 \times 10^{4})$
	BP2	$1.76 \times 10^{0}(1.76 \times 10^{3})$	$0.76 \times 10^{0}(7.64 \times 10^{3})$	$0.20 \times 10^{0}(2.02 \times 10^{4})$
	BP3	$0.12 \times 10^{0}(1.23 \times 10^{2})$	$9.50 \times 10^{-2}(9.50 \times 10^{2})$	$2.80 \times 10^{-2}(2.80 \times 10^{3})$
	BP4	$0.18 \times 10^{0}(1.79 \times 10^{2})$	$9.05 \times 10^{-1}(9.05 \times 10^{3})$	$3.46 \times 10^{-1}(3.46 \times 10^{4})$
	bkgs	$1.57 \times 10^{0}(1.57 \times 10^{3})$	$1.59 \times 10^{0}(1.59 \times 10^{4})$	$2.97 \times 10^{0}(2.67 \times 10^{5})$
$N_R N_R + Z(\to \ell\ell)Z(\to \ell\ell)$	BP1	$3.53 \times 10^{-2}(3.53 \times 10^{1})$	$2.29 \times 10^{-2}(2.29 \times 10^{2})$	$7.21 \times 10^{-3}(7.21 \times 10^{2})$
	BP2	$0.98 \times 10^{0}(9.80 \times 10^{2})$	$0.75 \times 10^{0}(7.54 \times 10^{3})$	$0.24 \times 10^{0}(2.42 \times 10^{4})$
	BP3	$3.23 \times 10^{-2}(3.23 \times 10^{1})$	$7.87 \times 10^{-2}(7.87 \times 10^{2})$	$3.08 \times 10^{-2}(3.08 \times 10^{3})$
	BP4	$7.50 \times 10^{-3}(7.50 \times 10^{0})$	$0.39 \times 10^{0}(3.89 \times 10^{3})$	$0.30 \times 10^{0}(3.02 \times 10^{4})$
	bkgs	$1.08 \times 10^{-1}(1.08 \times 10^{2})$	$1.39 \times 10^{-1}(1.39 \times 10^{3})$	$3.74 \times 10^{-1}(3.36 \times 10^{4})$
$N_R N_R + V(\to q\bar{q})V(\to q\bar{q})$	BP1	$1.05 \times 10^{1}(1.05 \times 10^{4})$	$6.57 \times 10^{0}(6.57 \times 10^{4})$	$2.02 \times 10^{0}(2.02 \times 10^{5})$
	BP2	$2.76 \times 10^{0}(2.76 \times 10^{3})$	$2.08 \times 10^{0}(2.08 \times 10^{4})$	$0.65 \times 10^{0}(6.57 \times 10^{4})$
	BP3	$8.90 \times 10^{-2}(8.90 \times 10^{1})$	$2.15 \times 10^{-1}(2.15 \times 10^{3})$	$8.30 \times 10^{-2}(8.30 \times 10^{3})$
	BP4	$1.30 \times 10^{-2}(1.30 \times 10^{1})$	$9.74 \times 10^{-1}(9.74 \times 10^{3})$	$7.96 \times 10^{-1}(7.96 \times 10^{4})$
	bkgs	$6.63 \times 10^{1}(6.63 \times 10^{4})$	$1.71 \times 10^{2}(1.71 \times 10^{6})$	$3.34 \times 10^{2}(3.01 \times 10^{7})$
$N_R N_R + H_{\rm SM}(\to b\bar{b})H_{\rm SM}(\to b\bar{b})$	BP1	$1.21 \times 10^{0}(1.21 \times 10^{3})$	$1.12 \times 10^{0}(1.12 \times 10^{4})$	$3.77 \times 10^{-1}(3.77 \times 10^{4})$
	BP2	$3.95 \times 10^{-1}(3.95 \times 10^{2})$	$5.29 \times 10^{-1}(5.29 \times 10^{3})$	$1.88 \times 10^{-1}(1.88 \times 10^{4})$
	BP3	$1.22 \times 10^{-2}(1.22 \times 10^{1})$	$5.32 \times 10^{-2}(5.32 \times 10^{2})$	$2.36 \times 10^{-2}(2.36 \times 10^{3})$
	BP4	$1.40 \times 10^{-3}(1.40 \times 10^{0})$	$2.49 \times 10^{-1}(2.49 \times 10^{3})$	$2.27 \times 10^{-1}(2.27 \times 10^{4})$
	bkgs	$6.63 \times 10^{1}(6.63 \times 10^{4})$	$1.71 \times 10^{2}(1.71 \times 10^{6})$	$3.34 \times 10^{2}(3.01 \times 10^{7})$

We note that the background originated from the production of two W bosons can be significantly reduced by using the requirement that there are two SFOS leptons whose invariant mass is close to the Z-boson mass. The backgrounds can further be reduced by imposing cuts on the so-called transverse mass m_{T2} computed from the dilepton and missing energy system. Given that the missing transverse energy of the background comes from the decay of the Z boson, further improvements can be obtained by optimizing the transverse mass of both the leading and the subleading lepton with the missing energy defined as $m_T^{\rm max}$ and $m_T^{\rm min}$,

$$m_T^{\rm max} = \sqrt{p_{T,\ell}^{\rm lead} p_T^{\rm miss}(1-\cos\Delta\phi_1)},$$
$$m_T^{\rm min} = \sqrt{p_{T,\ell}^{\rm slead} p_T^{\rm miss}(1-\cos\Delta\phi_2)}, \quad (38)$$

where $p_{T,\ell}^{\rm lead}$ ($p_{T,\ell}^{\rm slead}$) is the transverse momentum of the leading (subleading) charged lepton, and $\Delta\phi_1(\Delta\phi_2)$ is the difference in the azimuthal angle between the leading (subleading) charged lepton the vector of the transverse missing momentum. In Table III, we show the cross sections for the signal and the backgrounds and the expected number of events for 3, 10, and 30 TeV center-of-mass energies. We can see that the signal-to-background ratio is already good[12] for most of the benchmark points, which varies between 10^{-3} and about 10^{-1}. This makes the $\ell\ell + E_T^{\rm miss}$ final state one of the most promising channels to discover dark matter signals at muon colliders.

$N_R N_R + Z(\to q\bar{q})$ and $N_R N_R + H_{\rm SM}(\to b\bar{b})$.—This category of channels involves two hadronic jets in association with missing energy. For the case of the Z boson, the main decay channel is into $q\bar{q}; q = u, d, s, c, b$ with ${\rm BR}(Z \to q\bar{q}) = 69.911\%$ [135]. For the SM Higgs boson, the main decay is into $b\bar{b}$ with ${\rm BR}(H_{\rm SM} \to b\bar{b}) = 57\%$.

[12]Note that this signal-to-background ratio is estimated at the matrix-element generation level where we do not define any cuts on the final-state objects. The signal-to-background ratio that we found for most of the benchmark points and processes simply implies that a careful analysis would lead to a high potential discovery of this model at future muon colliders, which we report for future works.

The dominant backgrounds to these signal processes come from $q\bar{q}$ production in association with two neutrinos, SM Higgs boson production, $t\bar{t}$ production with one top quark decaying leptonically and the other top decaying hadronically, and WW production where one W-boson decays leptonically and the other decays hadronically. The total cross section for the backgrounds can be approximated by

$$\sigma(q\bar{q}+E_T^{\rm miss}) \approx \sigma(q\bar{q}+\nu\bar{\nu}) + \sigma(WZ)\times {\rm BR}(Z\to\nu\bar{\nu}) \times {\rm BR}(W\to q\bar{q}) + 2\sigma(t\bar{t})\times {\rm BR}(t\to b\ell\nu) \times {\rm BR}(t\to bq\bar{q}), \quad (39)$$

where $\sigma(q\bar{q}+\nu\bar{\nu})$ includes all the irreducible backgrounds that consist of the production of $H_{\rm SM}Z$ and ZZ, where one particle decays invisibly and the other particle decays hadronically. The last three backgrounds contribute when the leading charged lepton escapes the detection. Since both the hadronically decaying Z and Higgs bosons are accompanied with very large missing energy, their decays are not always resolved as two well-separated jets, but rather as fat jets with specific characteristics. We expect these channels to yield good statistics and the signal-to-background ratio varies between 10^{-4} and 10^{-2}. Note that, for the mono-Higgs channel, the signal-to-background ratio becomes extremely small at 30 TeV.

2. $\mu^+\mu^- \to N_R N_R + XY$

$N_R N_R+\gamma\gamma$.—There is also the possibility to produce a pair of DM particles in association with two hard photons. The expected final state would consist of two hard photons in addition to large missing energy. Contrary to the mono-γ channel, this process does not have large backgrounds where its main components are the resonant (via the decay of the SM Higgs) and nonresonant production of two photons in association with two neutrinos. The estimated background is given by

$$\sigma(\gamma\gamma+E_T^{\rm miss}) \approx \sigma(H+X)\times {\rm BR}(H\to\gamma\gamma) + \sigma(\gamma\gamma+\nu\bar{\nu}). \quad (40)$$

The resonant background can be easily suppressed via suitable requirements on the invariant mass of the diphoton system, i.e., by removing photons that are within the SM Higgs mass window. The signal-to-background ratios are really large for this channel, varying between 10^{-3} and 10^{-1} for most of the benchmark points.

$N_R N_R+\gamma Z(\to \ell\ell)$.—This is also one of the unique processes for probing DM at muon colliders. The final state consists of one hard photon, two charged leptons, and large missing transverse energy. The associated background is manageable since it consists of the production of one photon and two gauge bosons. The total cross section for the background is given by

$$\sigma(\gamma\ell\ell+E_T^{\rm miss}) \approx 2\sigma(\gamma ZZ)\times {\rm BR}(Z\to\nu\bar{\nu})\times {\rm BR}(Z\to\ell\ell) + \sigma(\gamma WW)\times {\rm BR}(W\to\ell\nu)^2. \quad (41)$$

The expected number of signal events is quite large as well, i.e., of about $\mathcal{O}(10^2$–$10^4)$, while the number of background events is of similar size.

$N_R N_R + Z(\to \ell\ell)Z(\to \ell\ell)$.—This is one of the cleanest final states that can be used to probe DM at muon colliders. The signature consists of four charged leptons in association with missing energy. The corresponding background is even smaller than for the other signal processes. We note that enough statistics can only be achieved at $\sqrt{s_{\mu\mu}}=10$, 30 TeV where we expect about $\mathcal{O}(10^2$–$10^4)$ events. The major backgrounds arise from the production of three gauge bosons or from the production of the SM Higgs boson decaying into $VV^*, V=W,\ Z$ in association with one or two gauge bosons. The backgrounds that arose from the production of the SM Higgs boson are negligibly small as compared to those coming from triboson production. The total cross section is given as

$$\sigma(\ell\ell\ell\ell+E_T^{\rm miss}) \approx 3\sigma(ZZZ)\times {\rm BR}(Z\to\ell\ell)^2 \times {\rm BR}(Z\to\nu\bar{\nu}) + \sigma(WWZ) \times {\rm BR}(W\to\ell\nu)^2\times {\rm BR}(Z\to\ell\ell). \quad (42)$$

The signal-to-background ratio is found to be ≥ 1 for BP2 and BP4 at 10 TeV (see Table IV).

$N_R N_R + V(\to q\bar{q})V(\to q\bar{q})$ *and* $N_R N_R + H_{\rm SM}(\to b\bar{b})\times H_{\rm SM}(\to b\bar{b})$.—The production of two gauge bosons or two SM Higgs bosons in association with DM pairs leads to either four resolved jets or two fat jets in association with large missing energy. The dominant backgrounds for these signal processes consist of the production of two SM neutrinos in association with two gauge bosons, two SM Higgs bosons, or one Higgs boson and one gauge boson decaying hadronically. The cross section for the background processes is given by

$$\sigma(qq\bar{q}\,\bar{q}+E_T^{\rm miss}) \approx \sum_{ij}[\sigma(V_iV_j)\times {\rm BR}(V_i\to q\bar{q}) \times {\rm BR}(V_j\to q\bar{q})] + 2\sigma(t\bar{t}) \times {\rm BR}(t\to bqq)\times {\rm BR}(t\to b\nu\ell), \quad (43)$$

where the diboson production (V_iV_j) only contributes in the VBF mode through charged current with two forward neutrinos.

VI. PRODUCTION OF CHARGED SCALARS AT MUON COLLIDERS

In this section, we discuss the production of charged scalar pairs at muon colliders. Similar to the production of DM, charged scalars can be produced either in association with one SM particle, with two SM particles, or three SM particles. In addition, we could have the production of charged scalar pairs with non-SM particles ($H^{\pm}H^{\pm}$) or the production of four charged scalars. An interesting feature about the production of charged scalars is the appearance of at least two leptons in association with missing energy in addition to the decay products of the SM particles. For example, the production of charged scalar pairs in association with a SM Higgs boson would lead to two hard charged leptons, missing energy, and two b-tagged jets (or one fat jet). On the other hand, the charged scalar production receives contributions from VBF thanks to their coupling to γ/Z. The results of the production cross sections for the different processes involving charged

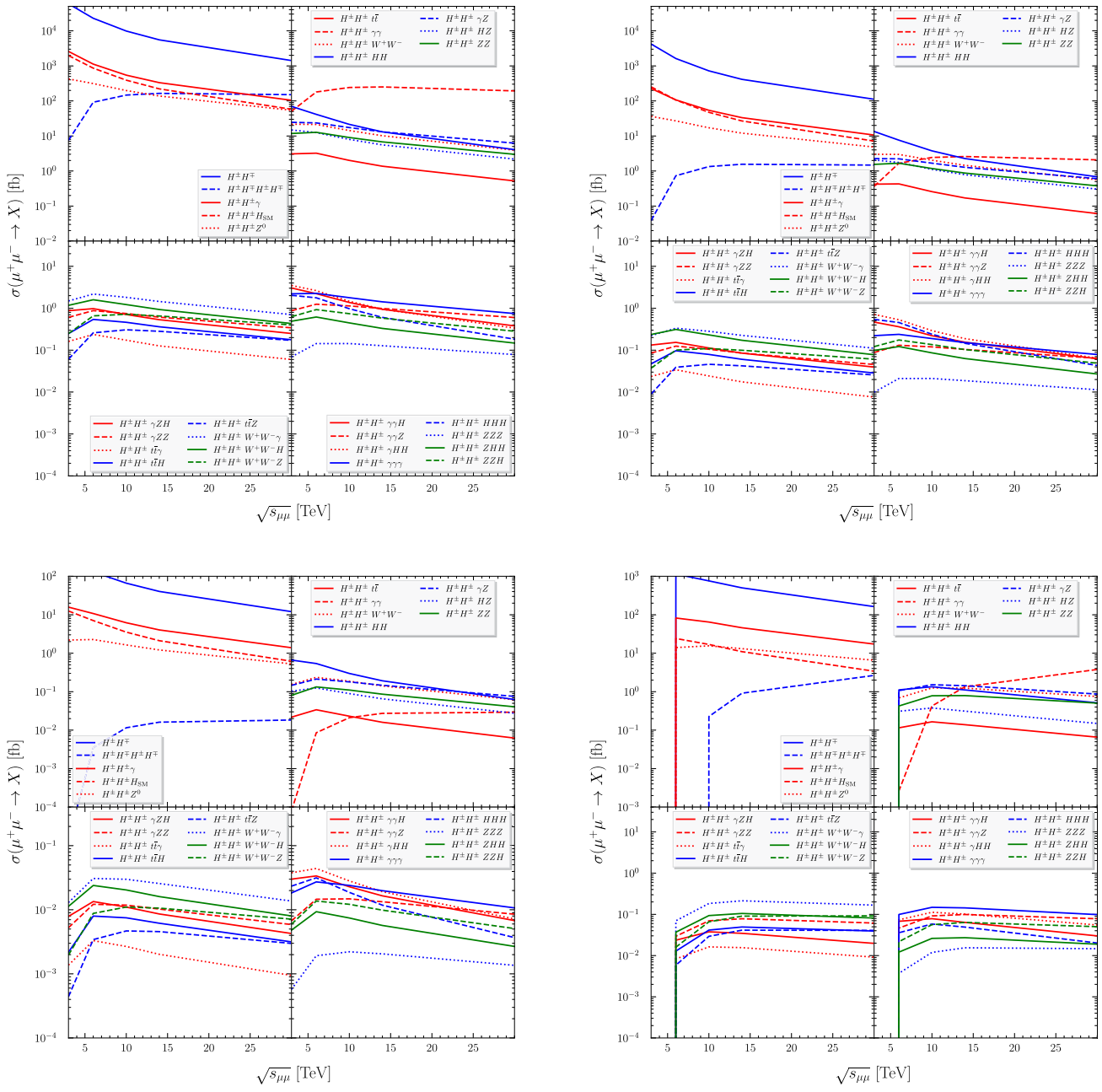

FIG. 8. Production cross section of $H^{\pm}H^{\mp} + X$ as a function of the center-of-mass energy ($\sqrt{s_{\mu\mu}}$) for the benchmark points BP1 (left upper panel), BP2 (right upper panel), BP3 (left lower panel), and BP4 (right lower panel). For each pane, we show the production cross section for $H^{\pm}H^{\mp}$ plus one SM particle, plus two SM particles, and in association with three SM particles.

scalars as a function of the center-of-mass energy are shown in Fig. 8. Below, we list the possible production channels for the charged scalars:

$\mu\mu \to H^{\pm}H^{\mp}/H^{\pm}H^{\mp}H^{\pm}H^{\mp}$.—These processes lead to signatures of either two charged leptons and missing transverse energy (MET) or four charged leptons and MET. Charged scalar pair production proceeds through either s-channel diagrams with the exchange of γ/Z bosons or t-channel diagrams with the exchange of the Majorana DM. The cross section for charged scalar pair production ranges from about 10^4 fb to about 10^1 fb. It is worth noting that for the benchmark point BP3 has the smallest cross section due to the tiny mass splitting of about 2 GeV between the charged scalar and the DM candidate. In all the cases, the number of events for this process is quite large. The cross section for charged scalar pair production has a $1/\sqrt{s_{\mu\mu}}$ scaling. The cross section for the production of four charged scalars is smaller as expected due to phase suppression. It is, however, quite decent as can be seen in Fig. 8 and ranges from 10^{-2} to 10^2 fb depending on the benchmark scenarios. The most notable signatures are four muons plus MET (BP1, BP2, BP3) and two muons and two tau leptons (BP4). These two channels will be studied in great detail in a future work [136].

$\mu\mu \to H^{\pm}H^{\mp} + X$.—In this case, we have three production channels: $H^+H^-\gamma$, H^+H^-Z, and $H^+H^-H_{\rm SM}$. There are three contributions to $H^+H^-\gamma$: s-channel contributions through γ/Z with the photon being emitted from the H^+H^- vertex and t-channel contribution through the exchange of N_R. The final-state signature for this process consists of two charged leptons in association with one hard photon (the kinematics is quite different from $N_RN_R\gamma Z$ production). We can see in Fig. 8 that the cross section ranges from 10^1 to 10^3 fb depending on the center-of-mass energy and the benchmark point. Second, we can have the production of charged scalar pairs in association with one Z boson, which would lead to very rich signatures: 2ℓ + MET, 2ℓ + 2 jets + MET, or 4ℓ + MET. The cross sections for these processes are shown in Fig. 8 where it is clear that the rates are quite important from 10^0 to 10^2 fb. Finally, the charged scalar pairs can be produced in association with a SM Higgs boson. The rates for this interesting channel are also quite important and range between 10^0 and 10^2 fb.

$\mu\mu \to H^{\pm}H^{\mp} + XY$.—For this category, we have seven production channels: $H^+H^-\gamma\gamma$, $H^+H^-\gamma Z$, H^+H^-ZZ, $H^+H^-W^+W^-$, $H^+H^-H_{\rm SM}H_{\rm SM}$, $H^+H^-H_{\rm SM}Z$, and $H^+H^-t\bar{t}$. The rates for these channels are quite a bit smaller, but still at the noticeable level, i.e., from 10^{-2} to 10^2 fb depending on the center-of-mass energy and the benchmark point. It is worth noting that the production of charged scalar pairs in association with two SM particles leads to even richer signatures with very small backgrounds, i.e., six leptons plus MET, four leptons plus four jets plus MET, and so on.

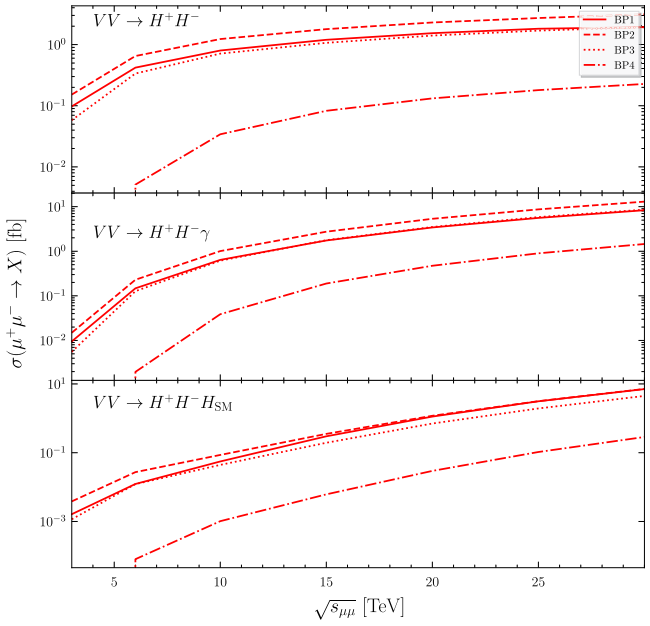

FIG. 9. The production cross sections for H^+H^-, $H^+H^-\gamma$, and $H^+H^-H_{\rm SM}$ through VBF as a function of the center-of-mass energy ($\sqrt{s_{\mu\mu}}$) for BP1 (solid), BP2 (dashed), BP3 (dotted), and BP4 (dash-dotted).

$\mu\mu \to H^{\pm}H^{\mp} + XYZ$.—This is the most complicated category of processes, where we can have 16 processes with many more final-state signatures. The rates for these processes are much smaller with the maximum being about 3 fb for $H^+H^-\gamma H_{\rm SM}H_{\rm SM}$ and $H^+H^-\gamma\gamma H_{\rm SM}$ at $\sqrt{s_{\mu\mu}} = 3$ TeV.

We close this section with a brief discussion of the contribution of VBF to the production of charged scalars in this model. As mentioned earlier, the charged scalar couples to the photon and the Z boson and therefore may receive pure gauge VBF contributions to the total production cross section. In this model, we can have the production of charged scalars through $\gamma\gamma H^+H^-$, γZH^+H^-, ZZH^+H^-, $ZZ \to H_{\rm SM} \to H^+H^-$, and $W^+W^- \to \gamma/Z \to H^+H^-$ vertices. We take examples of production of H^+H^-, $H^+H^-\gamma$, and $H^+H^-H_{\rm SM}$ and show the corresponding results for the four benchmark points in Fig. 9. We can see that the cross sections increase with center-of-mass energy, but do not go above 2 fb for H^+H^- in BP2. Therefore, the muon annihilation channels are the most important in our model thanks to the $Y_{\mu N}^4$ dependence of the cross section.

VII. CONCLUSIONS

In this work, we have studied the production of DM and charged scalars at high-energy muon colliders within the minimal lepton portal DM model. The model consists of extending the SM with two $SU(2)_L$ gauge singlets: a charged singlet scalar and a neutral right-handed fermion (or, equivalently, a Majorana fermion). We first discussed in

detail the phenomenology of the model at the LHC and the corresponding constraints from direct detection, relic density measurement, and lepton flavor violating decays of charged leptons and the SM Higgs boson. Then we selected a few benchmark points that define some phenomenologically viable scenarios and which can be tested at future muon colliders. For these benchmark points, we have calculated the cross sections for the production of DM in association with SM particles and of charged scalars of the models in association with SM particles as a function of the center-of-mass energy. For DM production in association with SM particles, we have studied the total rates of 26 possible channels for the benchmark points considered in this study. Furthermore, we studied the total number of events and the associated backgrounds for nine prominent channels and found that they are very important for the discovery of DM at muon colliders for masses up to ∼1 TeV. We furthermore analyzed the production of charged scalar production in association with SM particles (about 28 channels). The potential discovery for DM through charged scalar production at muon colliders is also as interesting as for direct production of DM. Further investigations of this model at muon colliders are ongoing, where a full signal-to-background optimization will be carried out for a number of selected channels.

ACKNOWLEDGMENTS

The work of A. J. is supported by the Institute for Basic Science (IBS) under the project code IBS-R018-D1. The work of S. N. is supported by the United Arab Emirates University (UAEU) under UPAR Grant No. 12S093.

[1] G. Jungman, M. Kamionkowski, and K. Griest, Phys. Rep. **267**, 195 (1996).
[2] L. Bergström, Rep. Prog. Phys. **63**, 793 (2000).
[3] G. Bertone, D. Hooper, and J. Silk, Phys. Rep. **405**, 279 (2005).
[4] J. L. Feng, Annu. Rev. Astron. Astrophys. **48**, 495 (2010).
[5] P. A. R. Ade *et al.* (Planck Collaboration), Astron. Astrophys. **594**, A13 (2016).
[6] M. Beltran, D. Hooper, E. W. Kolb, Z. A. C. Krusberg, and T. M. P. Tait, J. High Energy Phys. 09 (2010) 037.
[7] L. M. Carpenter, A. Nelson, C. Shimmin, T. M. P. Tait, and D. Whiteson, Phys. Rev. D **87**, 074005 (2013).
[8] N. F. Bell, J. B. Dent, A. J. Galea, T. D. Jacques, L. M. Krauss, and T. J. Weiler, Phys. Rev. D **86**, 096011 (2012).
[9] A. Berlin, T. Lin, and L.-T. Wang, J. High Energy Phys. 06 (2014) 078.
[10] G. Aad *et al.* (ATLAS Collaboration), Phys. Rev. D **103**, 112006 (2021).
[11] G. Aad *et al.* (ATLAS Collaboration), J. High Energy Phys. 11 (2021) 209.
[12] G. Aad *et al.* (ATLAS Collaboration), J. High Energy Phys. 04 (2021) 165.
[13] A. M. Sirunyan *et al.* (CMS Collaboration), J. High Energy Phys. 03 (2020) 025.
[14] A. M. Sirunyan *et al.* (CMS Collaboration), Eur. Phys. J. C **81**, 13 (2021); **81**, 333(E) (2021).
[15] E. Aprile *et al.* (XENON Collaboration), Phys. Rev. Lett. **121**, 111302 (2018).
[16] X. Cui *et al.* (PandaX-II Collaboration), Phys. Rev. Lett. **119**, 181302 (2017).
[17] P. Athron *et al.* (GAMBIT Collaboration), Eur. Phys. J. C **77**, 568 (2017).
[18] P. Athron *et al.* (GAMBIT Collaboration), Eur. Phys. J. C **77**, 879 (2017).
[19] M. J. Baker *et al.*, J. High Energy Phys. 12 (2015) 120.
[20] S.-M. Choi, Y.-J. Kang, H. M. Lee, and T.-G. Ro, J. High Energy Phys. 10 (2018) 104.
[21] K. A. Mohan, D. Sengupta, T. M. P. Tait, B. Yan, and C. P. Yuan, J. High Energy Phys. 05 (2019) 115.
[22] G. Belanger *et al.*, J. High Energy Phys. 02 (2022) 042.
[23] B. Belfatto, D. Buttazzo, C. Gross, P. Panci, A. Strumia, N. Vignaroli, L. Vittorio, and R. Watanabe, J. High Energy Phys. 06 (2022) 084.
[24] J. Liu, B. Shuve, N. Weiner, and I. Yavin, J. High Energy Phys. 07 (2013) 144.
[25] Y. Bai and J. Berger, J. High Energy Phys. 08 (2014) 153.
[26] S. Chang, R. Edezhath, J. Hutchinson, and M. Luty, Phys. Rev. D **90**, 015011 (2014).
[27] P. Agrawal, Z. Chacko, and C. B. Verhaaren, J. High Energy Phys. 08 (2014) 147.
[28] M. Garny, A. Ibarra, and S. Vogl, Int. J. Mod. Phys. D **24**, 1530019 (2015).
[29] J. Kawamura, S. Okawa, and Y. Omura, J. High Energy Phys. 08 (2020) 042.
[30] A. Jueid, S. Nasri, and R. Soualah, J. High Energy Phys. 04 (2021) 012.
[31] S. Okawa and Y. Omura, J. High Energy Phys. 02 (2021) 231.
[32] S.-I. Horigome, T. Katayose, S. Matsumoto, and I. Saha, Phys. Rev. D **104**, 055001 (2021).
[33] J. Liu, X.-P. Wang, and K.-P. Xie, J. High Energy Phys. 06 (2021) 149.
[34] S. Iguro, S. Okawa, and Y. Omura, J. High Energy Phys. 03 (2023) 010.
[35] B. Díaz Sáez and K. Ghorbani, J. Cosmol. Astropart. Phys. 02 (2023) 002.
[36] J. Kawamura, S. Okawa, and Y. Omura, Phys. Rev. D **106**, 015005 (2022).
[37] J. P. Delahaye, M. Diemoz, K. Long, B. Mansoulié, N. Pastrone, L. Rivkin, D. Schulte, A. Skrinsky, and A. Wulzer, arXiv:1901.06150.

[38] K. Long, D. Lucchesi, M. Palmer, N. Pastrone, D. Schulte, and V. Shiltsev, Nat. Phys. **17**, 289 (2021).
[39] H. Al Ali *et al.*, Rep. Prog. Phys. **85**, 084201 (2022).
[40] A. Costantini, F. De Lillo, F. Maltoni, L. Mantani, O. Mattelaer, R. Ruiz, and X. Zhao, J. High Energy Phys. 09 (2020) 080.
[41] R. Ruiz, A. Costantini, F. Maltoni, and O. Mattelaer, J. High Energy Phys. 06 (2022) 114.
[42] R. Capdevilla, D. Curtin, Y. Kahn, and G. Krnjaic, Phys. Rev. D **103**, 075028 (2021).
[43] M. Chiesa, F. Maltoni, L. Mantani, B. Mele, F. Piccinini, and X. Zhao, J. High Energy Phys. 09 (2020) 098.
[44] T. Han, Y. Ma, and K. Xie, Phys. Rev. D **103**, L031301 (2021).
[45] T. Han, Z. Liu, L.-T. Wang, and X. Wang, Phys. Rev. D **103**, 075004 (2021).
[46] W. Yin and M. Yamaguchi, Phys. Rev. D **106**, 033007 (2022).
[47] G.-y. Huang, F. S. Queiroz, and W. Rodejohann, Phys. Rev. D **103**, 095005 (2021).
[48] R. Capdevilla, D. Curtin, Y. Kahn, and G. Krnjaic, Phys. Rev. D **105**, 015028 (2022).
[49] R. Capdevilla, F. Meloni, R. Simoniello, and J. Zurita, J. High Energy Phys. 06 (2021) 133.
[50] P. Asadi, R. Capdevilla, C. Cesarotti, and S. Homiller, J. High Energy Phys. 10 (2021) 182.
[51] M. Casarsa, M. Fabbrichesi, and E. Gabrielli, Phys. Rev. D **105**, 075008 (2022).
[52] W. Liu, K.-P. Xie, and Z. Yi, Phys. Rev. D **105**, 095034 (2022).
[53] T. Han, S. Li, S. Su, W. Su, and Y. Wu, Phys. Rev. D **104**, 055029 (2021).
[54] T. Han, Y. Ma, and K. Xie, J. High Energy Phys. 02 (2022) 154.
[55] T. Han, W. Kilian, N. Kreher, Y. Ma, J. Reuter, T. Striegl, and K. Xie, J. High Energy Phys. 12 (2021) 162.
[56] G.-S. Lv, X.-M. Cui, Y.-Q. Li, and Y.-B. Liu, Nucl. Phys. **B985**, 116016 (2022).
[57] J. Liu, Z.-L. Han, Y. Jin, and H. Li, J. High Energy Phys. 12 (2022) 057.
[58] A. Azatov, F. Garosi, A. Greljo, D. Marzocca, J. Salko, and S. Trifinopoulos, J. High Energy Phys. 10 (2022) 149.
[59] J.-C. Yang, X.-Y. Han, Z.-B. Qin, T. Li, and Y.-C. Guo, J. High Energy Phys. 09 (2022) 074.
[60] Y. Bao, J. Fan, and L. Li, J. High Energy Phys. 08 (2022) 276.
[61] S. Chen, A. Glioti, R. Rattazzi, L. Ricci, and A. Wulzer, J. High Energy Phys. 05 (2022) 180.
[62] S. Homiller, Q. Lu, and M. Reece, J. High Energy Phys. 07 (2022) 036.
[63] S. Baum, P. Sandick, and P. Stengel, Phys. Rev. D **102**, 015026 (2020).
[64] B. Swiezewska and M. Krawczyk, Phys. Rev. D **88**, 035019 (2013).
[65] A. Arhrib, R. Benbrik, and N. Gaur, Phys. Rev. D **85**, 095021 (2012).
[66] A. Jueid, J. Kim, S. Lee, S. Y. Shim, and J. Song, Phys. Rev. D **102**, 075011 (2020).
[67] G. Aad *et al.* (ATLAS, CMS Collaborations), J. High Energy Phys. 08 (2016) 045.
[68] G. C. Branco, P. M. Ferreira, L. Lavoura, M. N. Rebelo, M. Sher, and J. P. Silva, Phys. Rep. **516**, 1 (2012).
[69] S. Kanemura, T. Kubota, and E. Takasugi, Phys. Lett. B **313**, 155 (1993).
[70] A. G. Akeroyd, A. Arhrib, and E.-M. Naimi, Phys. Lett. B **490**, 119 (2000).
[71] I. F. Ginzburg, K. A. Kanishev, M. Krawczyk, and D. Sokolowska, Phys. Rev. D **82**, 123533 (2010).
[72] OPAL Collaboration, Eur. Phys. J. C **32**, 453 (2004).
[73] G. Aad *et al.* (ATLAS Collaboration), Eur. Phys. J. C **80**, 123 (2020).
[74] G. Aad *et al.* (ATLAS Collaboration), Phys. Rev. D **101**, 052005 (2020).
[75] R. D. Ball *et al.* (NNPDF Collaboration), J. High Energy Phys. 04 (2015) 040.
[76] M. L. Mangano, M. Moretti, F. Piccinini, and M. Treccani, J. High Energy Phys. 01 (2007) 013.
[77] L. M. Krauss, S. Nasri, and M. Trodden, Phys. Rev. D **67**, 085002 (2003).
[78] E. Ma, Phys. Rev. D **73**, 077301 (2006).
[79] A. Ahriche, A. Jueid, and S. Nasri, Phys. Rev. D **97**, 095012 (2018).
[80] S. Baumholzer, V. Brdar, and P. Schwaller, J. High Energy Phys. 08 (2018) 067.
[81] D. Borah, P. S. B. Dev, and A. Kumar, Phys. Rev. D **99**, 055012 (2019).
[82] T. Kitabayashi, Phys. Rev. D **98**, 083011 (2018).
[83] A. Ahriche, A. Arhrib, A. Jueid, S. Nasri, and A. de La Puente, Phys. Rev. D **101**, 035038 (2020).
[84] S. Baumholzer, V. Brdar, P. Schwaller, and A. Segner, J. High Energy Phys. 09 (2020) 136.
[85] D. Borah, A. Dasgupta, K. Fujikura, S. K. Kang, and D. Mahanta, J. Cosmol. Astropart. Phys. 08 (2020) 046.
[86] M. Sarazin, J. Bernigaud, and B. Herrmann, J. High Energy Phys. 12 (2021) 116.
[87] J. Hisano, T. Moroi, K. Tobe, and M. Yamaguchi, Phys. Rev. D **53**, 2442 (1996).
[88] E. Arganda and M. J. Herrero, Phys. Rev. D **73**, 055003 (2006).
[89] A. Ilakovac, A. Pilaftsis, and L. Popov, Phys. Rev. D **87**, 053014 (2013).
[90] T. Toma and A. Vicente, J. High Energy Phys. 01 (2014) 160.
[91] J. Adam *et al.* (MEG Collaboration), Phys. Rev. Lett. **110**, 201801 (2013).
[92] A. M. Baldini *et al.*, arXiv:1301.7225.
[93] B. Aubert *et al.* (*BABAR* Collaboration), Phys. Rev. Lett. **104**, 021802 (2010).
[94] K. Hayasaka (Belle, Belle-II Collaborations), J. Phys. Conf. Ser. **408**, 012069 (2013).
[95] U. Bellgardt *et al.* (SINDRUM Collaboration), Nucl. Phys. **B299**, 1 (1988).
[96] A. Blondel *et al.*, arXiv:1301.6113.
[97] K. Hayasaka *et al.*, Phys. Lett. B **687**, 139 (2010).
[98] A. M. Sirunyan *et al.* (CMS Collaboration), Phys. Rev. D **104**, 032013 (2021).
[99] V. Khachatryan *et al.* (CMS Collaboration), Phys. Lett. B **763**, 472 (2016).
[100] M. Tanabashi *et al.* (Particle Data Group), Phys. Rev. D **98**, 030001 (2018).

[101] J. Herrero-Garcia, N. Rius, and A. Santamaria, J. High Energy Phys. 11 (2016) 084.
[102] R. J. Scherrer and M. S. Turner, Phys. Rev. D **33**, 1585 (1986); **34**, 3263(E) (1986).
[103] K. Griest and D. Seckel, Phys. Rev. D **43**, 3191 (1991).
[104] F. Ambrogi, C. Arina, M. Backovic, J. Heisig, F. Maltoni, L. Mantani, O. Mattelaer, and G. Mohlabeng, Phys. Dark Universe **24**, 100249 (2019).
[105] C. Amole *et al.* (PICO Collaboration), Phys. Rev. Lett. **118**, 251301 (2017).
[106] M. Cirelli, E. Del Nobile, and P. Panci, J. Cosmol. Astropart. Phys. 10 (2013) 019.
[107] R. J. Hill and M. P. Solon, Phys. Rev. D **91**, 043505 (2015).
[108] F. Bishara, J. Brod, B. Grinstein, and J. Zupan, J. High Energy Phys. 11 (2017) 059.
[109] J. Ellis, N. Nagata, and K. A. Olive, Eur. Phys. J. C **78**, 569 (2018).
[110] M. Backović, A. Martini, O. Mattelaer, K. Kong, and G. Mohlabeng, Phys. Dark Universe **9–10**, 37 (2015).
[111] H. H. Patel, Comput. Phys. Commun. **197**, 276 (2015).
[112] E. Aprile *et al.* (XENON Collaboration), J. Cosmol. Astropart. Phys. 11 (2020) 031.
[113] D. S. Akerib *et al.* (LZ Collaboration), Phys. Rev. D **101**, 052002 (2020).
[114] C. E. Aalseth *et al.* (DarkSide-20k Collaboration), Eur. Phys. J. Plus **133**, 131 (2018).
[115] J. Billard, L. Strigari, and E. Figueroa-Feliciano, Phys. Rev. D **89**, 023524 (2014).
[116] G. Passarino and M. Veltman, Nucl. Phys. **B160**, 151 (1979).
[117] T. Hahn and M. Perez-Victoria, Comput. Phys. Commun. **118**, 153 (1999).
[118] T. Hahn, Comput. Phys. Commun. **140**, 418 (2001).
[119] G. Aad *et al.* (ATLAS Collaboration), J. High Energy Phys. 11 (2015) 206.
[120] V. Khachatryan *et al.* (CMS Collaboration), J. High Energy Phys. 02 (2017) 135.
[121] A. M. Sirunyan *et al.* (CMS Collaboration), Phys. Lett. B **793**, 520 (2019).
[122] G. Belanger, B. Dumont, U. Ellwanger, J. F. Gunion, and S. Kraml, Phys. Rev. D **88**, 075008 (2013).
[123] J. Ellis and T. You, J. High Energy Phys. 06 (2013) 103.
[124] Projected performance of Higgs analyses at the HL-LHC for ECFA 2016, Technical Report No. CMS-PAS-FTR-16-002, CERN, Geneva, 2017.
[125] O. Cerri, M. de Gruttola, M. Pierini, A. Podo, and G. Rolandi, Eur. Phys. J. C **77**, 116 (2017).
[126] D. M. Asner *et al.*, arXiv:1310.0763.
[127] M. Dong *et al.* (CEPC Study Group), arXiv:1811.10545.
[128] M. Selvaggi, Proc. Sci. ICHEP2018 (**2019**) 684.
[129] F. Staub, Comput. Phys. Commun. **185**, 1773 (2014).
[130] F. Staub, Comput. Phys. Commun. **182**, 808 (2011).
[131] J. Alwall, R. Frederix, S. Frixione, V. Hirschi, F. Maltoni, O. Mattelaer, H. S. Shao, T. Stelzer, P. Torrielli, and M. Zaro, J. High Energy Phys. 07 (2014) 079.
[132] C. Degrande, C. Duhr, B. Fuks, D. Grellscheid, O. Mattelaer, and T. Reiter, Comput. Phys. Commun. **183**, 1201 (2012).
[133] A. Jueid and S. Nasri (to be published).
[134] M. Belfkir, A. Jueid, and S. Nasri (to be published).
[135] R. L. Workman *et al.* (Particle Data Group), Prog. Theor. Exp. Phys. **2022**, 083C01 (2022).
[136] M. Belfkir, A. Jueid, and S. Nasri (to be published).